ELECTRIC FIELD CALCULATION AND IONIZATION SIGNAL SIMULATION IN LIQUID XENON DETECTORS FOR PET

by

Huang Zhu

B.E., Huazhong University of Science and Technology, 2008

A THESIS SUBMITTED IN PARTIAL FULFILLMENT OF

THE REQUIREMENTS FOR THE DEGREE OF

MASTER OF SCIENCE

in

THE FACULTY OF GRADUATE STUDIES

(Physics)

THE UNIVERSITY OF BRITISH COLUMBIA

(Vancouver)

February 2012

Abstract

Electric field calculations and ionization signal simulations in a liquid xenon detector for Positron Emission Tomography have been performed. The electric field was calculated using Opera 3D, a Finite Element Method application software. The uniformity of the electric field inside of the detector was evaluated by calculating the deviation of drifting electrons under the applied electric field. The ionization signals of the detector have been simulated. The comparison between simulation results and measurement signals was made.

Table of Contents

List of Tables

List of Figures

Acknowledgements

I would like to acknowledge my supervisor Professor Douglas Bryman for his patience and guidance over the last 2 years. He is the most respectable person I have ever met in my life. Without his consistent support and care, I couldn't have been achieving this far.

Another person I would like to give my special thanks is Alice Miceli. Her altitude on daily scientific research always inspires me. She is always ready to help others. Her encourage is always so warm when I meet any difficulties. Furthermore, I want to say thanks to Fabrice Retiere and Pierre Amaudruz for their help on my ionization signals simulation and slow control system design. I also really appreciate the colleagues in our lab, Leonid Kurchaninov, Ray Bula and Charles Mcconnell Clement. Their guidance and advice are also significant for my research.

In addition, many thanks to the staff at Triumf and UBC, without their work, I wouldn't have such a convenient environment for study. I also want to thank Professor Colin Gay for his help on my thesis review, Professor Alex Mackay for his leadership in the Medical Physics program, and the course instructors in UBC and BCCA.

Lastly, I would like to express my sincerest gratitude to my family and closest friends. They let me know love is actually all around.

Dedication

This thesis is dedicated to my mother. She said simple words to me the when I was a child, which turns out to be so powerful today. She is always there to support and comfort me, and never allows me to give up.

Chapter 1: Introduction

In modern medical research and clinical diagnosis, knowledge of anatomical information is not enough for understanding and diagnosing diseases. Functional information, which represents the metabolic activities *in vivo*, plays a more and more essential role to reveal biological processes and related pathologies. Therefore, Positron Emission Tomography (PET), as a functional scanning technique, has attracted more and more attention in recent years. PET technology has also been improving by employing new detector materials and techniques. However, the image quality of conventional PET is still limited in spatial resolution and signal-to-noise ratio. The liquid xenon (LXe) PET project is aiming to develop a new type of PET detector with better spatial resolution, sensitivity, and signal-to-noise ratio. This thesis will introduce the current challenges in PET imaging, and the potential LXe has for improving the performance of current PET system as a well-known γ ray detection medium. In the next chapters, the calculation results of electric field inside a LXe PET detector prototype will be described. A method for simulating signals of ionization electron clouds in the detector will be presented.

1.1 Positron Emission Tomography

Positron Emission Tomography (PET) is widely used for diagnosing early stage cancer in hospitals nowadays. PET is also an advanced and powerful tool for the research of cardiovascular and nervous system diseases such as coronary heart disease and Parkinsonism (1) (2), as its unique capability of mapping the metabolic activity in heart and brain.

To conduct a PET scan, a short-lived radioisotope, which is chemically combined with a biologically active molecule, is injected into the cardiovascular system of a patient. This radioactive tracer is absorbed by various organs and tissues depending on their individual metabolic level. The most common tracer in clinical use is fluorodeoxyglucose (FDG), a combination of ^{18}F and glucose. Its half life is about 110 minutes. The radioisotope undergoes positron emission decay in organs or tissues, emitting a positron. Electron–positron annihilation occurs when the positron interacts with an electron, producing a pair of back to back 511 keV γ rays. When the γ rays reach a typical PET detector consisting of a dense inorganic scintillating crystal like LSO (3) segmented for obtaining spatial resolution, a burst of scintillation photons is generated and detected by photon detection devices such as a photomultiplier or avalanche photodiode. The detection and localization of the two back to back γ rays in coincidence forms a line of response, or LOR. The source of the annihilation is located at a certain point along this LOR. A large data set of LORs is used for reconstructing a PET image which describes the distribution of radioactive tracers in the patients' body. In modern clinical application, PET usually functions in combination with x-ray computed tomography (CT), providing precise anatomic localization and functional imaging, which has already revolutionized many fields of medical diagnosis (4).

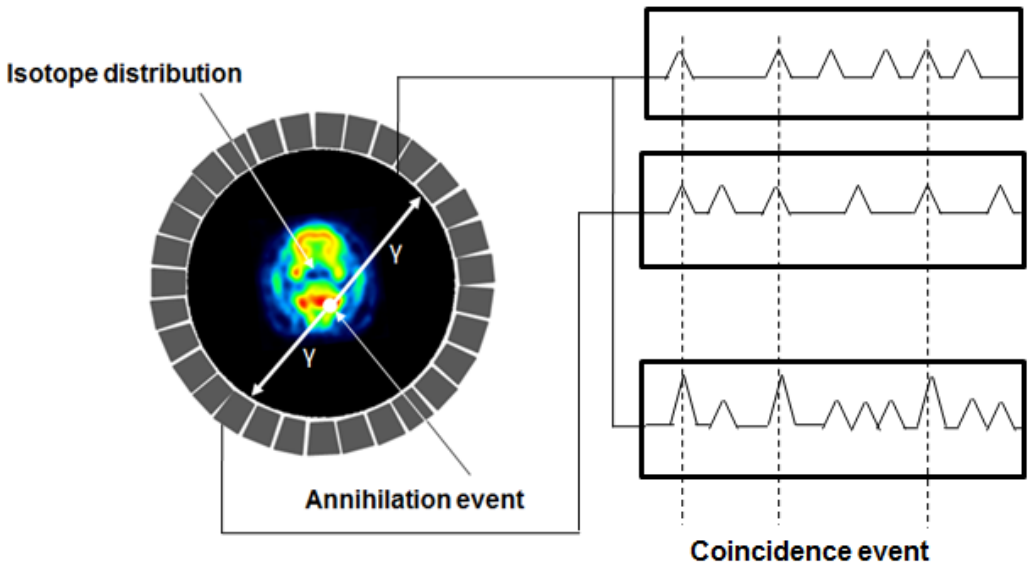

Figure 1 Typical PET system. A ring of detectors record single γ-ray events. When single events occur within a short time window, they are considered in coincidence and saved as a coincident event (5).

1.2 Challenges of PET

1.2.1 Spatial Resolution

The goal of PET is to generate images of the distribution of radioactive tracer in the patient's body. The spatial resolution of PET imaging is limited by three factors. The first factor is positron range. Before electron-positron annihilation occurs, positrons travel a short distance in human tissue, which limit the localization of the source. For ^{18}F, the positron range in water is 1.2 mm (6). Second, the motion of the electron immediately prior to annihilation causes an angular uncertainty in the direction of the 511-keV photons that is approximately 4 mrad (0.23 °) from exact collinearity (6)(7). And for a detector ring with a typical diameter 80 cm, resolution loss due to non-collinearity of annihilation γ rays is 1.7 mm (6). Positron range and non-collinearity are intrinsic physical limitations of PET giving maximum requirements on spatial resolution of reconstructed images (8). The third significant factor is the intrinsic spatial resolution of the PET detector, typically 2-5 mm (9). The resolution of a

single detector is quantified by the full width at half-maximum (FWHM) of the position distribution obtained by placing a collimated point source in front of the detector at a fixed distance. In order to achieve better intrinsic spatial resolution, scintillation crystals used in conventional PET should be segmented into smaller sizes, since the point spread function (PSF) for a single detector is similar to a step function with a total width equal to the size of crystals. However, it should also be noted that the crystal size should not be too small because of surface imperfection worsens the sensitivity and energy resolution of the system. Some typical spatial resolutions of current PET scanners from different manufacturers are given in Table 1, including Discovery ST of GE (10), ECAT ACCEL of CTI-Siemez (11), Gemini TF of Philips (12). Some other small animal scanners have resolution less than 2mm at the center of the field of view (13)(14).

	Discovery ST (GE)	ECAT ACCEL (CTI-Siemenz)	Gemini TF (Philips)
Transaxial Resolution			
FWHM (mm) at 1cm	6.7	6.2	4.8
FWHM (mm) at 10 cm	7.9	7.2	5.2
Axial Resolution			
FWHM (mm) at 1cm	6.7	5.7	4.8
FWHM (mm) at 10 cm	7.6	6.7	5.2

Table 1 Spatial resolution performance of conventional PET systems in clinical use.

1.2.2 Signal to Noise Ratio

A major challenge is to reduce the noise in PET images. A significant source of noise in PET images comes from inclusion of incorrect coincidence events. There are three types of coincidence events in PET, which are detected by two detectors within the time window

(usually in the magnitude of nanoseconds): true coincidences, scattered coincidences, and random coincidences. In true coincidences, gamma rays from one positron-electron annihilation form a LOR without any scatter in the patient. In scattered coincidences, one or both gamma rays scatter within the patient, which is the significant source of noise in PET image. Random coincidence results from the detection of gamma rays from different annihilation events which are close enough in time to satisfy the coincidence requirement. Figure 2 illustrates three kinds of coincidence events for PET imaging. The true coincidence and scatter coincidence rate are related linearly to the activity of radioisotope in the patient. The random coincidence rate increases as the square of the activity in the patient, and becomes dominant at higher activity levels. Our goal in PET imaging is to measure and accurately reconstruct the distribution from true coincidences while minimizing the scattered and random coincidences.

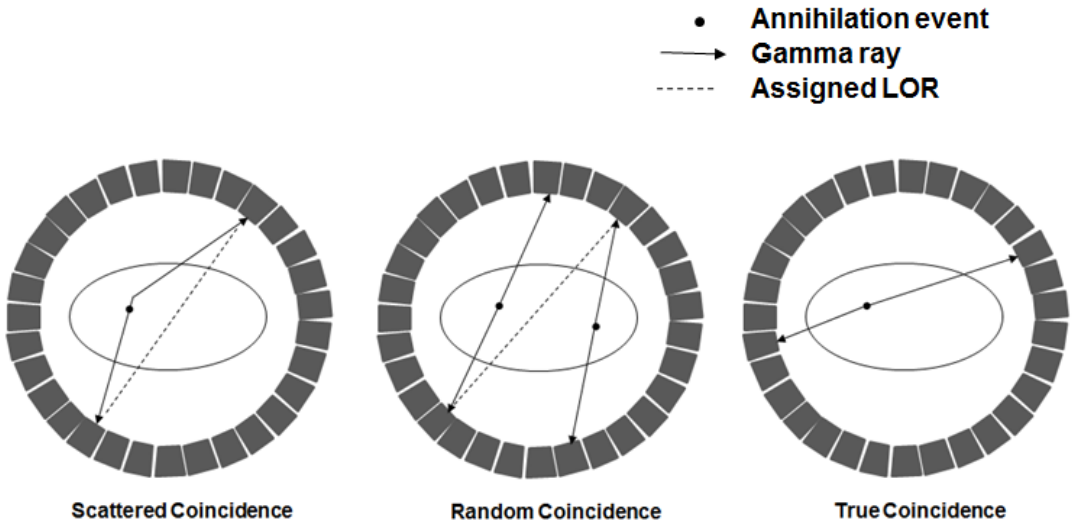

Figure 2 Three types of coincidence measured in PET system: true coincidence, random coincidence and scattered coincidence (6).

Another limitation in imaging is referred to as parallax error, which results from the uncertainty of depth of interaction (DOI) of the 511 keV γ rays. In conventional PET detectors, the γ rays travel unknown distances in the detection medium before being completely absorbed. Then, if the gamma rays enter the crystal at an oblique angle, the crystal of the interaction may not be the same as the one first entered (See Figure 3). Thus, unless the DOI within a crystal can be accurately determined, an incorrect LOR will be assigned to the interaction causing blurring.

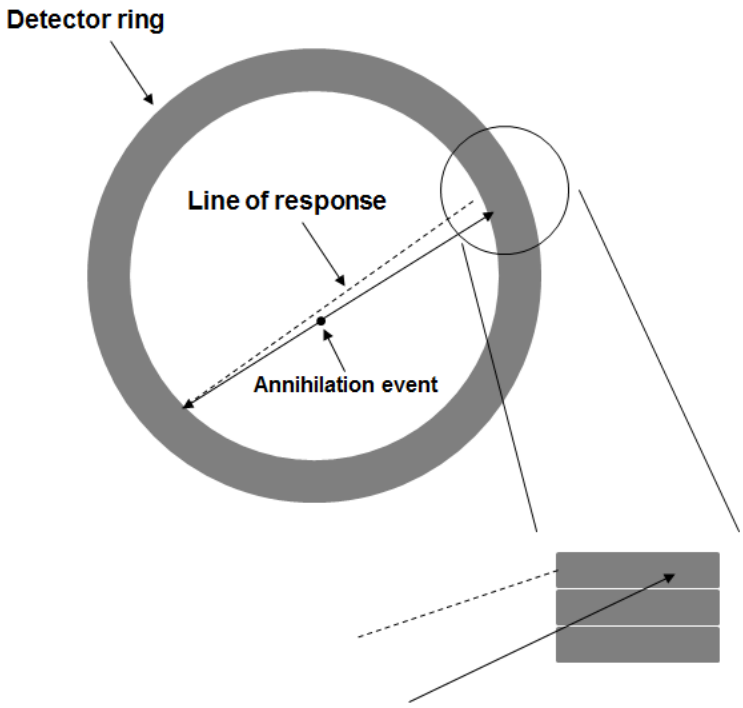

Figure 3 Parallax error. The γ ray interacts in a crystal which is not the first one it entered with. An incorrect LOR will be assigned to this interaction (6).

In order to reduce noise and increase the detected true coincidence events in PET, a number of approaches have been explored. One method for increasing true coincidence events is to increase activity of radioisotope. However, this method has been proved to be not practical,

since the random coincidence rate increases much faster than the true and scatter coincidence rates at higher radioisotope activity. Moreover, higher activity of radioisotope would result in higher radiation exposure to patients. Therefore, researchers are always looking for better scintillation materials with higher stopping power and faster response to build more sensitive detectors with shorter coincidence time window. Another approach is to use more of the energy spectrum to accept events with energy less than the photopeak. When low energy γ rays interact with matter it generates energetic electrons via three primary processes: photoelectric absorption, Compton scattering, and pair production. Generally, the majority of 511keV γ rays will scatter in the scintillator rather than be photoabsorbed. The photoelectric efficiencies of BGO, LSO, and NaI for 511 keV γ rays are 41%, 33%, and 18%, respectively (6). A lower energy window will capture those events with energies in the Compton region, which increase the number of scattered coincidences. Therefore, PET detectors with better energy resolution are able to decrease the contribution of scatter events and increases the number of true coincidence events. In an addition, the method of using Time of Flight in the image reconstruction algorithm has proved to be able to reduce the noise variance. Using Time of Flight information in reconstruction can constrain the positron position in a short line segment (7.5 cm for 500 ps time resolution); this technique was developed in the 1980s (15). This method became more promising in 2000s with the advent of new scintillation materials such as LSO. In (16), it has been shown that using time-of-flight (TOF) in the reconstruction algorithm can reduce the noise variance by a factor of 5 with 500 ps FWHM coincidence timing resolution in LSO-based PET detectors. In order to eliminate the parallax error in conventional scintillation PET, multiple layers of scintillation crystals were used for getting the depth of interaction (DOI) information must. Two layers or even four layers of

scintillation crystals DOI PET detectors were built for obtaining a sufficient positioning performance in (17)(18). However, this approach also increases the total cost of the system substantially.

1.3 Introduction to Liquid Xenon PET

LXe has been considered as a promising working medium for a PET since the 1970s (19) (20). Since the cross section of interactions of γ rays strongly depends on the density and atomic number of the detection medium, the 511 keV γ rays interact efficiently in LXe, because of the relatively high density (3.1 g/cm^3) and high atomic number (54) of LXe. LXe has exceptional characteristics as a scintillator: fast scintillation and large photon yield. The scintillation decay of LXe has two components: a slow decay of approximately 27 ns, and a fast decay of approximately 2.2 ns. The intensity ratio of the fast component to the slow components is 0.05 (21). The photon yield is 6.8 $x10^4$ photons/MeV at zero electric field with emission in the UV region (λ = 178 nm). In addition, compared to crystal scintillators, a unique and important feature of LXe is the production of ionization electrons, which can be detected under application of an electric field. The average energy per ion-pair (W = 15.6 eV) is relatively low. Table 2 lists some important physical properties of LXe. The proposed LXe PET detector discussed below attempts to take advantage of both the light and the charge signals for the detection of 511 keV annihilation photons.

	LXe
Atomic Number Z	54
Atomic Weight A	131.3
Density (g/cc)	3.1
Melting Point T_m (K)	161.4
Boiling Point T_b (K)	165.1
Critical Temperature T_c (K)	289.7
Critical Pressure P_c (atm)	57.64
Fano Factordfc	0.041
Drift Velocity (mm/μsec) @1 kV/cm	2.2
Radiation Length(cm)	2.77
(dE/dx)(MeV/cm)	3.89
W-value(eV) (scintillation) @ 0 kV/cm	14.7
W-value(eV) (ionization)	15.6
Wavelength of Scintillation Light (nm)	175
Decay const.	
fast(ns)	2.2
slow(ns)	27
Dielectric constant	1.95

Table 2 Physical properties of LXe (22).

The concept of LXe PET consists of a ring of twelve trapezoidal chambers filled with liquid xenon (24). Scintillation light is collected by large-area avalanche photodioes (LAAPD). There are 48 APDs in total for a single detector, arranged on opposing sides of the chamber (each side has 24 APDs). The fast decay time allows LXe to achieve < 1ns time resolution, which can reduce the random coincidences. Charge measurement is achieved using a time projection chamber (TPC) (23).

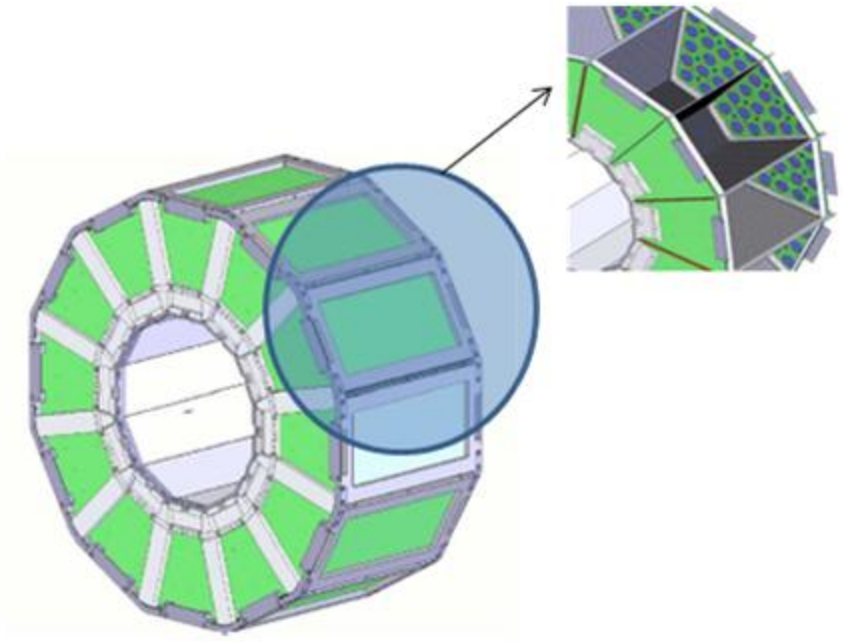

Figure 4 Conceptual LXe PET with twelve trapezoidal chambers (23).

Ionization electrons drift under an electric field applied between the cathode and the anode of the TPC. The anode module consists of a shielding grid, 96 induction wires and an anode which is segmented into 96 strips. The anode strips are perpendicular to the induction wires. The amplitudes of induced wire signals and collected strip signals depend on the X-Y distance of the electron cloud from individual wires and strips. Then, the coordinate of the electron cloud is determined by weighting the size of the signals induced on two wires and two strips, which gives precise X-Y coordinates of the interaction of the event inside the sensitive volume. The third coordinate Z is obtained by measuring the electron drift time. The scintillation light measured by the APDs provides the trigger both for readout of charge signals and coincidence measurements and it is used for fast localization of the position of the interaction at high rate. Ionization electrons drifting at approximately 2 mm/μs can take up to about 60μs to reach the anode plane, starting from the cathode. Hence, when the

interaction rate is larger than about 100 kHz, the location of the interaction must be reconstructed with the light with a precision of about 1cm in order to ensure proper matching between scintillation and ionization signals (24). A LXe PET detector prototype has been built in 2008 as shown in Figure 6.

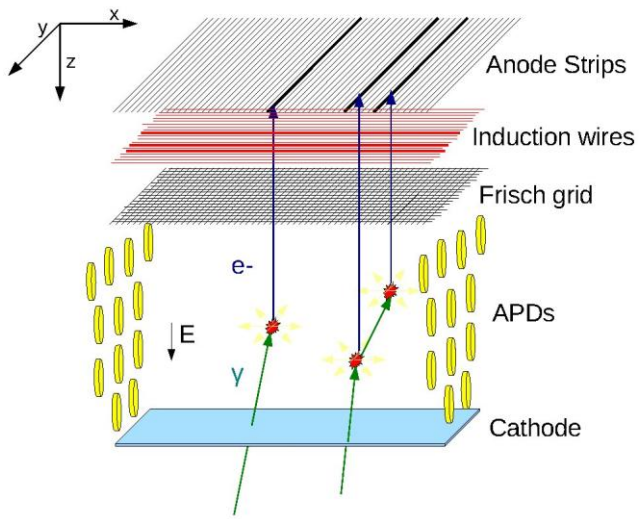

Figure 5 The schematic of TPC. Ionization electrons are drifted under an applied electric field. An array of induction wires and segmented anode provides two -dimensional positions of interactions with sub-millimeter precision (21).

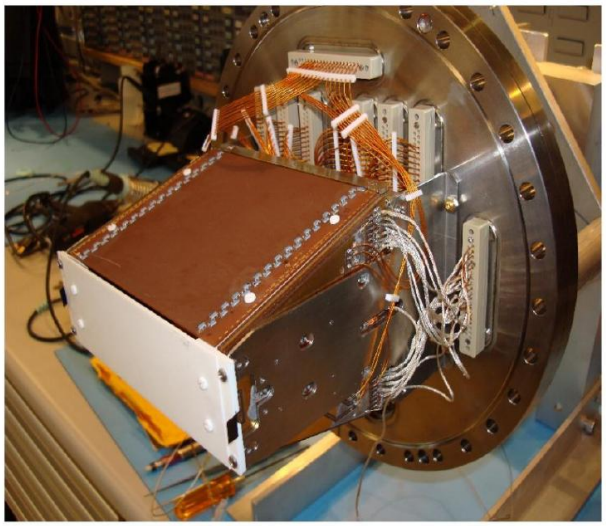

Figure 6 LXe PET sector prototype mounted on a flange (21).

The potential performance in terms of efficiency and image quality of a LXe PET compared to a crystal based system has been shown in simulations (24). The energy resolution was improved significantly by combining the information from light and charge using the anti-correlation of the two signals (24). The energy resolution measured from the combined spectrum can reach 4-7.5% FWHM, which is much better than 20-25% FWHM typical of conventional PET (25). Sub-millimeter (0.8mm) resolution of interaction location in 3 dimensions is another significant advantage over conventional PET both in terms of resolution and the ability to identify the exact location of interactions within the detector. Moreover, higher sensitivity can be achieved because of the large active volume of detection. Since every energy-depositing interaction is precisely recorded, Compton scattering can be reconstructed giving information on the direction of each incoming photon allowing suppression of random and scatter coincidences prior to reaching the detector (23).

Chapter 2: Electric Field Calculation

The accuracy of the position measurement of photon interactions largely depends on the uniformity of the electric field inside of the LXe TPC chamber. The electric field was calculated in Opera 3D (26), a Finite Element Analysis program, and the uniformity of the electric field was analyzed with ROOT (27). The core part of Opera 3D for the electrical field calculation is TOSCA. TOSCA computes magnetostatic and electrostatic fields in three dimensions, which is renowned for its accuracy of computation and has been proved by many years of industrial uses. ROOT is an object-oriented program and library developed at CERN. As a powerful data analysis framework, ROOT is widely used in many research facilities. In this work, ROOT is mainly for histogramming and graphing.

2.1 Purpose and Model Design

Information provided by the scintillation photons and ionization electrons can be used to locate the 3-dimensional position of interaction events within the LXe detector. Precise position allows an accurate LOR between two coincident events in a detector ring. Approximately 23000 ionization electrons are generated if the energy of a 511 keV γ ray is totally deposited in LXe detection medium for a typical electric field of 1 keV/cm. When the electric field is applied across the cathode and anode in the TPC, the electrons are drifted towards the anode. The induction wires and anode strips array detects the X-Y positions of these electrons. Assuming that the electric field is uniform in the X and Y direction, the X-Y position on the array is the same X-Y position where the electron was initially ionized. With constant and uniform field, Z position can be calculated by:

$$z = (t-t_0) \cdot v_d$$

where t is the time when ionization signals are detected on anode strips, and t_0 is the time when APDs are triggered by the scintillation light. v_d = (approximately) 2 mm/μs is the drift velocity, which is shown as function of electric field in Figure 7. Therefore, the uniformity of electric field is essential for 3-dimenstional position measurements of the interaction events in a LXe detector.

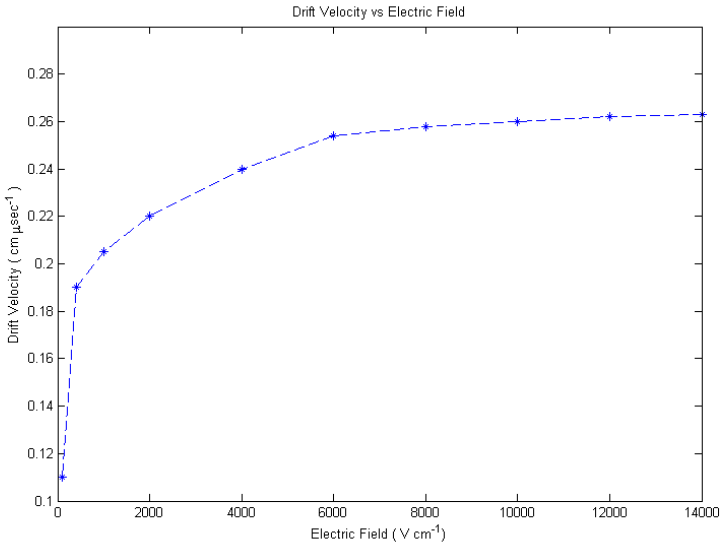

Figure 7 Drift velocity as a function of electric field (28).

A sector model for electric field calculations was built in Opera 3D. The important components in this model are the cathode plane, anode plane and field cage. In the LXe TPC, the anode module consists of 96 anode strips, 96 induction wires and a Frisch grid (29). Since this simulation is to calculate the electric field in the drift region, the anode module was simplified as an anode plane, and the anode strips, induction wires and grid were not modeled in the simulation. Both of the cathode and anode are single plates with 0.05mm thickness. The field cage in the sector consists of a series of 64 strips or 64 wires along the inside walls of the sector. The wires are in the planes of the APDs and strips are on the faces of the sector perpendicular to the APDs. Field cage strips are 0.05 mm thick, 0.75mm wide with a pitch of 1.77 mm while field cage wires have a dia. of 0.025 mm. The configuration of the sector is shown in Figure 8. The potential difference applied between the cathode and the anode used to perform electric field calculations is 20 kV. The anode plate is grounded, while the cathode plate is biased at -20 kV. The drift length of the sector is 11.3cm, so the expected

electric field in the drift region was 1770 V/cm. Each strip or wire in the field cage is biased so that it increases incrementally in potential from -20 kV at the cathode to 0 kV at the anode with constant increments, providing a uniform electric field in the drift region. The equation for calculating the potentials on the field cage strips is described as below (30):

$$V_{strip}(y) = \frac{-20kV * (D - y)}{D}$$

where $V_{strip}(y)$ is the potential on field cage strips (or wires), D is the distance between the anode and cathode, and y is the distance between field cage strips and cathode. The dielectric constant of LXe is set to 1.95 (22). A grounded box surrounds the chamber as well, representing the cryostat of the prototype.

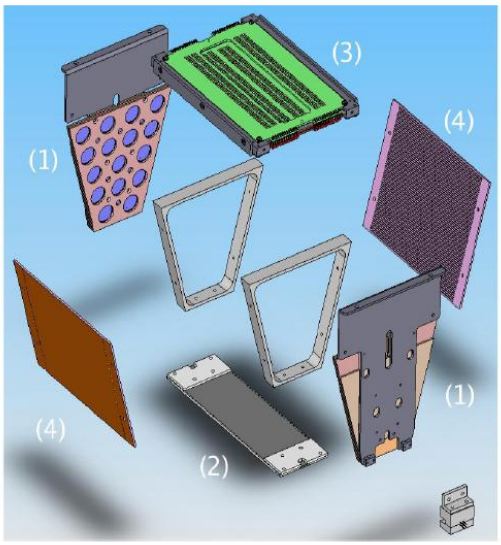

Figure 8 Elements in the sector: (1) APD (2) Cathode (3)Anode (4) Field cage

The geometry building and potential setting were done in the Modeller program of Opera 3D. The 3-dimensional model in Opera 3D is shown in Figure 9. These elements were all

immersed in LXe. The specifications of this model are outlined in the Table 3. The spacing of the electrodes is shown in Appendix A.

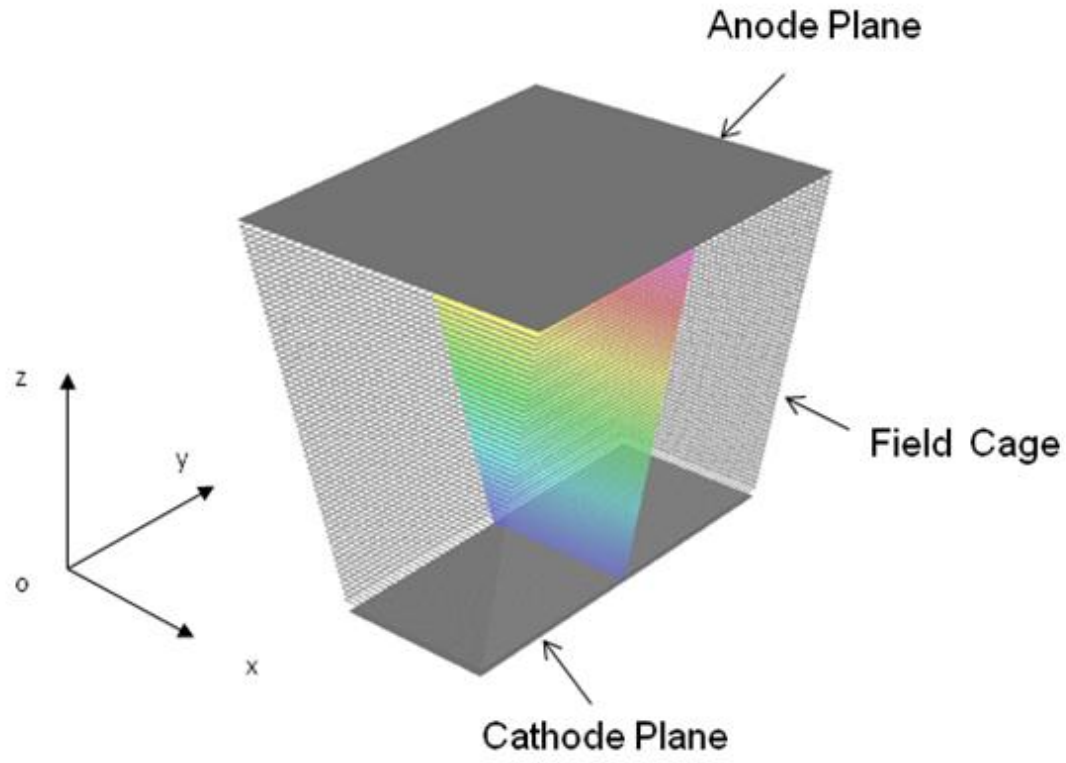

Figure 9 3 dimenstional model in Opera 3D, which consists a cathode (bottom), field cage strips around the chamber, and an anode (top).

Specifications in Opera 3D simulation model	
Distance between Cathode and Anode	113.1mm
Cathode Width and Length	52mm * 120mm
Cathode Thickness	0.005mm
Anode Width and Length	110mm * 120mm
Anode Thickness	0.005mm
Field Cage Wire Diameter	0.005mm
Field Cage Wire Length	Varies with distance to the cathode
Field Cage Strips Width and Length	1mm *120mm
Field Cage Strips thickness	0.002mm

Table 3 Specifications in Opera 3D simulation model.

After the sector model was built, the electric field analysis was done in the Post-Processor program of Opera 3D. The focus of this analysis is to determine the uniformity in the electric field in terms of its directionality and magnitude (31). The directionality of electric field will be investigated by how much the field lines deviate from ideal straight lines connecting the cathode and anode, which determines how far ionization electrons may deviate in the X-Y direction. The deviations in magnitude of the electric field component parallel to the drift axis determine how far an ionized electron may deviate along Z, the axis of drift.

2.2 Uniformity of Electric Field Magnitude

The magnitude of the component of the electric field parallel to the drift axis in the center plane of the detector is plotted in Figure 10. This indicates the effect that the electric field will have in altering an electron's drift. Most areas of the electric field are uniform with a

magnitude of 1770 V/cm at the center of the chamber. Irregularity increases towards the field cage, and the corner between the cathode and the first field cage strip and wire. Severe deformations in the electric field strength exist around the joint at the bottom. Here the electric field differs by approximately 1 kV/cm within a distance of 1 cm. This is not the characteristic of the entire chamber though, as the great majority of the electric field sites differ by less than 10 V/cm, approximately 0.5% of the field strength. The voltage on the same plane is plotted in Figure 11.

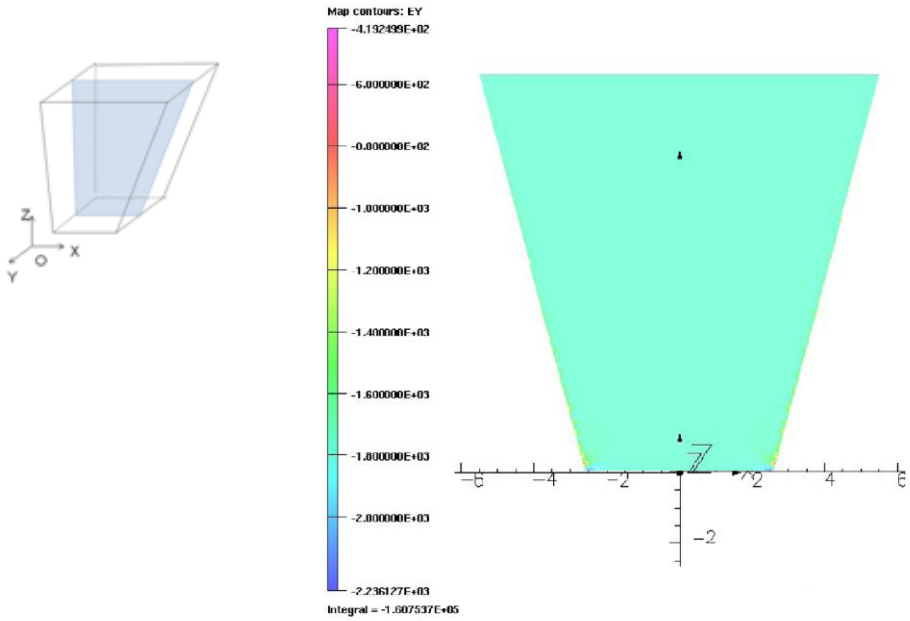

Figure 10 Component of the electric field parallel to the drift axis at the center of the chamber. Most of the area is uniform with magnitude of 1770 V/cm.

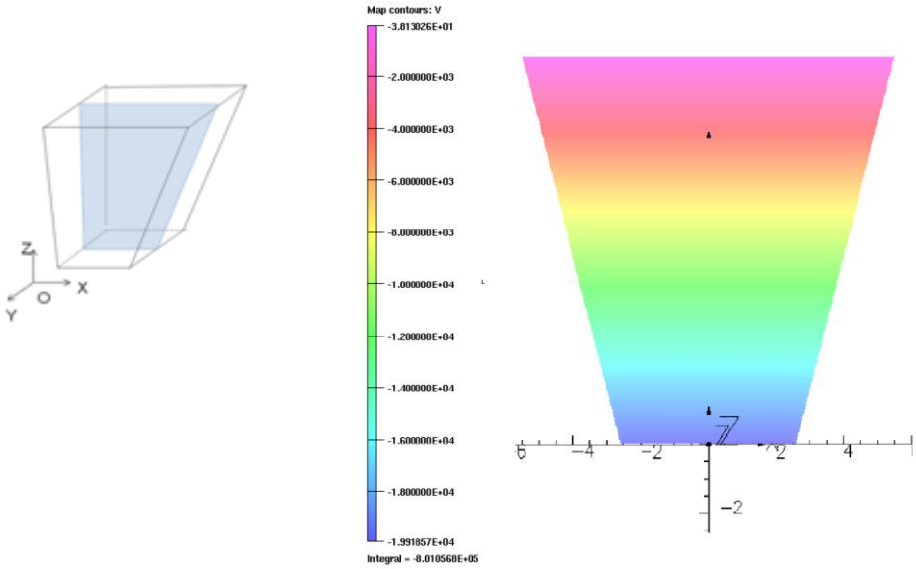

Figure 11 Voltage increased linearly with the distance to the cathode.

2.3 Uniformity of Electric Field Directionality

To investigate the directionality of the electric field, electrons were started from different starting points inside the sector to see how much they deviated when drifting towards to the anode plane. In Figure 12, the drifting electrons are shown as solid lines, which are actually a series of points with the step length of 0.1 mm, following the electric field lines.

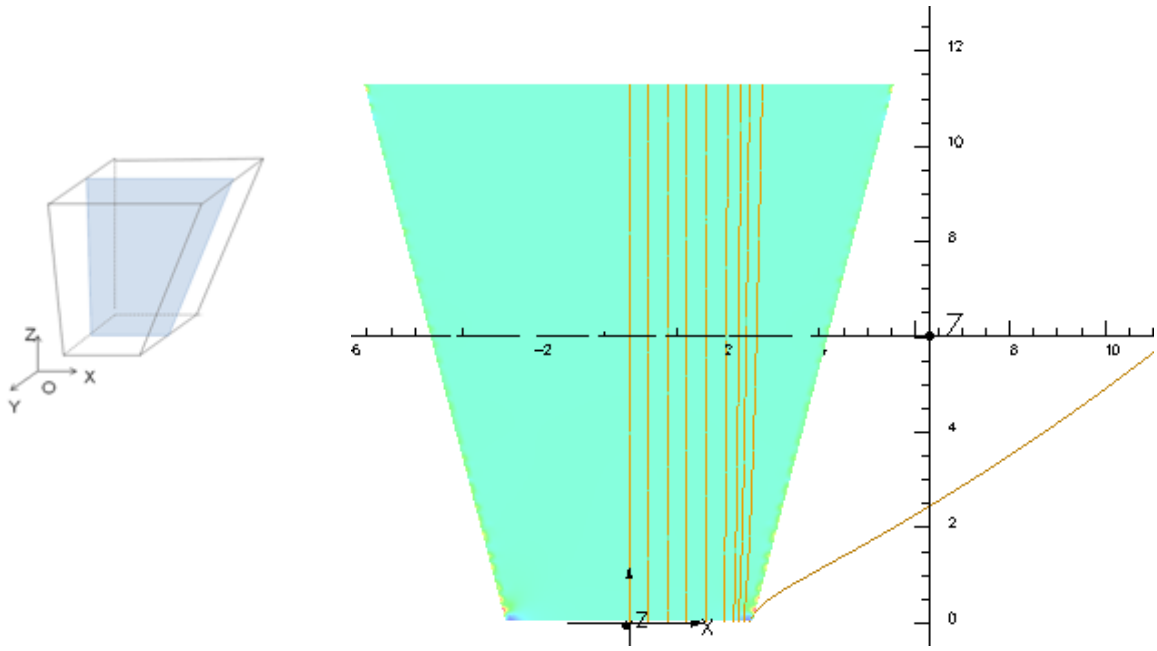

Figure 12 Drifting electrons are shown as solid lines, representing the direction of electric field lines.

A plot of the deviations along the X- axis of the field lines starting from the cathode towards to the anode is shown in Figure 13. It can be seen from this plot that the maximum deviation of any field line is less than 1 mm for nearly the entire plane. A small region, where field lines may deviate by more than 1mm, up to 3.8 mm, is between 22 mm and 24 mm from the center. This region is relatively small, comprising 7.7% of the horizontal axis. Electrons, which started in the region from 25 mm to 26 mm, drifted outside of the chamber. This region comprised 3.8% of the horizontal axis.

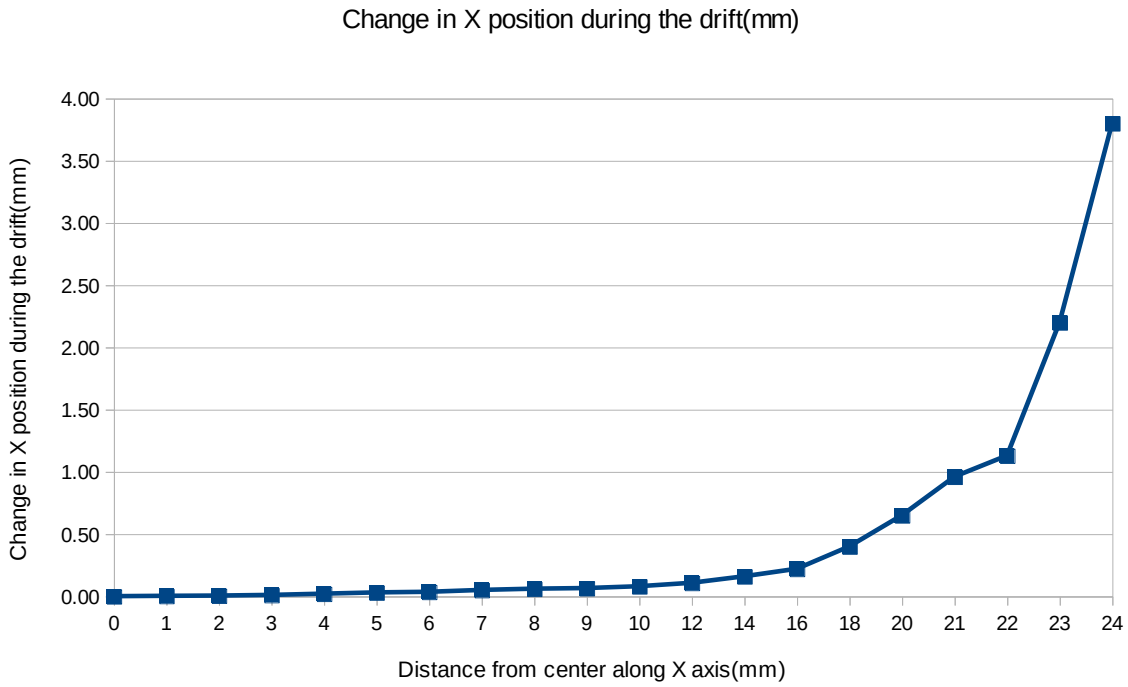

Figure 13 Deviation along x axis. Electrons started from the cathode plane.

Inside of the detector, the volume where electrons cannot reach the anode is called the dead space. No electrons ionized in this area will reach the anode, so no charge information can be used to reconstruct the positions of interaction from these interactions. The proportion of the dead space inside of the detector is a critical number for evaluating the charge collection performance of the detector. The volume, where the deviation of electron drifting is less than 1mm from the normal position, is called good volume. For the volume where the deviation is more than 1mm and is not dead space, calibration for the reconstruction of the positions of interaction is needed. In order to find the dead space and the good volume of the whole detector, 12 X-Z planes at different positions along Y-axis in the detector were sampled. On one single sampling plane, around 9000 electrons started at every 1mm*1mm

pixel, drift towards anode plane for calculating the deviation in the trapezoidal plane. In Figure 14, deviation contours of sampling planes at three different Y position are shown. The color scale represents the magnitude of the deviation at each pixel in this plane. Dead area in this plot was removed in this contour for better visualization. The region of dead space constitutes 3% of the total volume in this detector. The area where the deviation of drifting line is less than 1mm is for nearly the entire chamber, which constitutes 92% of the total volume. The deviations of each drifting electron were saved in text files for calibration.

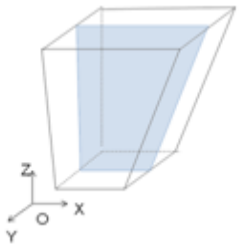

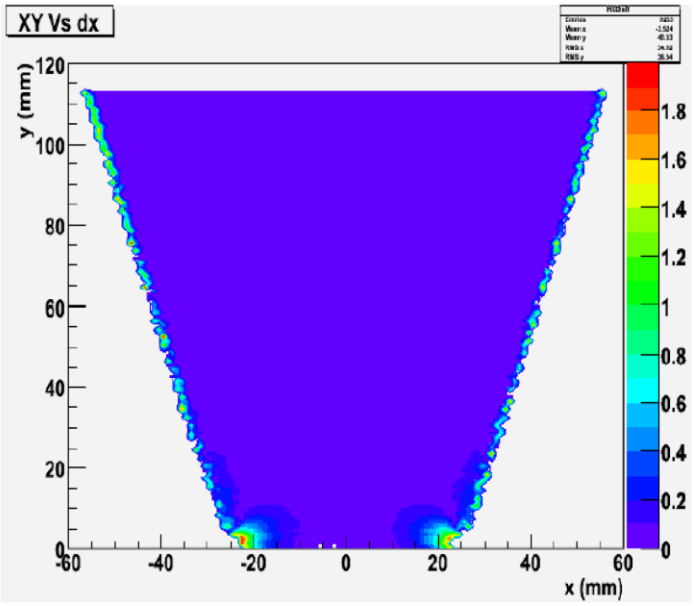

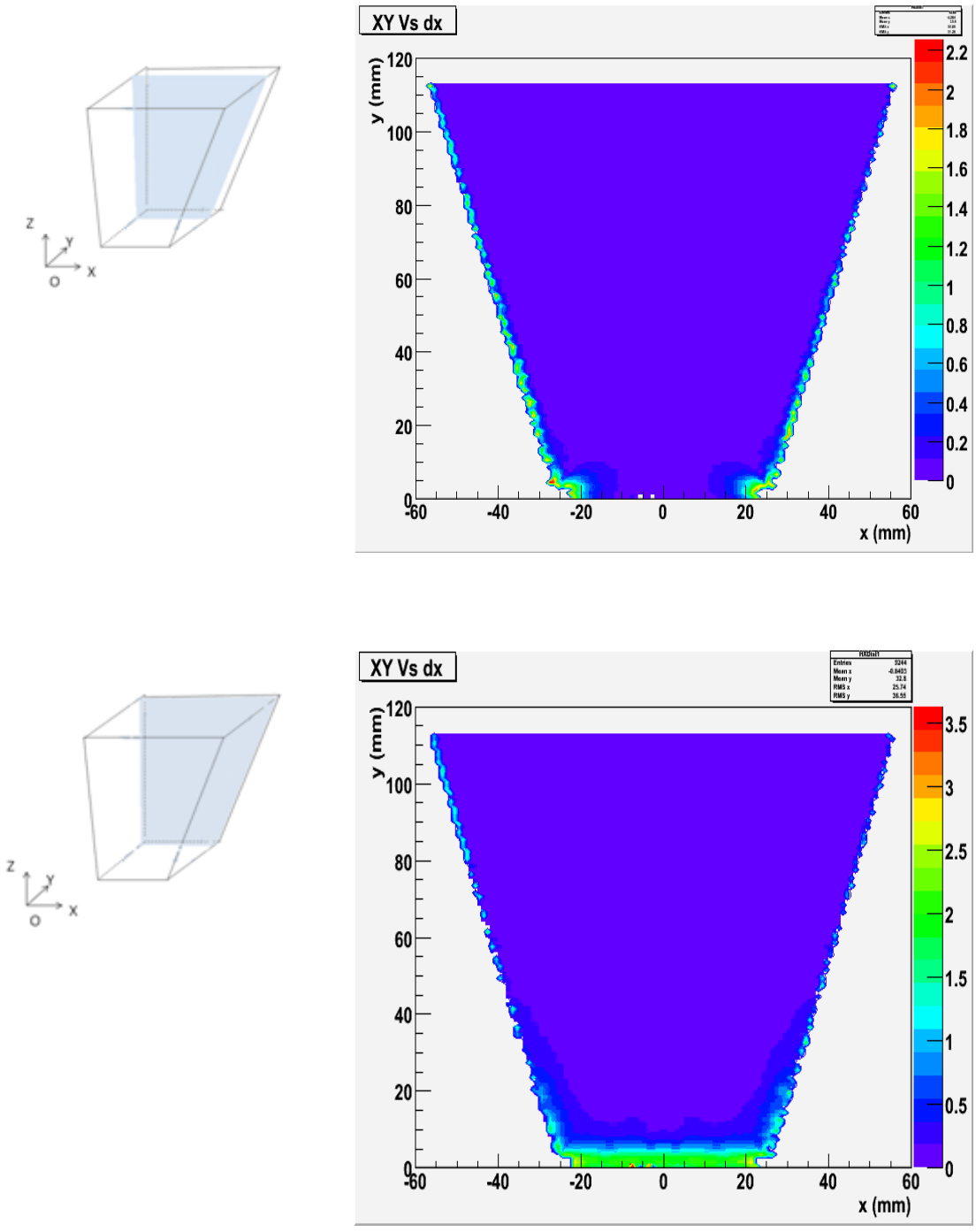

Figure 14 Deviation contour of the sampling planes at Y=0 mm, Y=30mm, Y = 55 mm (from top to bottom).

Chapter 3: Ionization Signal Simulation

One of the great advantages of LXe PET is its capability to take advantage of two types of information: scintillation light and ionization electrons, rather than the only scintillation information in conventional PET. The ionization electrons are measured with the TPC. By measuring the signals from the readout of the anode module in the TPC, we can get the 3D position information of the interaction events and also the energy information. Aiming to get better understanding about the measured signals in the prototype we built, ionization signals generated by 511keV γ ray in the LXe PET detector were simulated with Garfield (32) and further analysis was completed in Matlab (33). The comparison of the simulated signals and measured signals was made.

3.1 Ionization Signal in Time Projection Chamber

The anode module in TPC consists of a Frisch grid (29), induction wires and anode, which is shown in Figure 15. The Frisch shielding grid is a mesh, consisting of 0.03 mm dia. mesh wires spaced by 0.5 mm. The Frisch grid is placed between the cathode and the anode to shield the induction region from the electrons drifting in the grid-cathode region, and allows the current signal to be induced only after the electrons have crossed the grid. Since an electron induces a charge on the induction wires and the anode only after it passes the grid, all the electrons drift the same distance. Therefore the amplitudes of induced current pulses on the electrodes do not depend on the depth of the interaction, and it is only proportional to the total number of electron-ion pairs form along the trajectory of the primary ionizing particle, which gives the energy information of the interaction event in the chamber. The distance between the grid and induction wire plane is 1.6 mm. The induction wire plane consists of 96 induction wires with dia. of 0.05 mm spaced by 1.2 mm, and the induction wires are parallel with the grid wires. The anode is segmented into 96 anode strips located at 1.6 mm behind induction wire plane. Each strip has width of 1mm and thickness of 0.05 mm with a 0.25 mm separation with each other. The anode strips are perpendicular to the induction wires providing the second coordinate. The specifications of elements for the Garfield simulation are listed in Table 4.

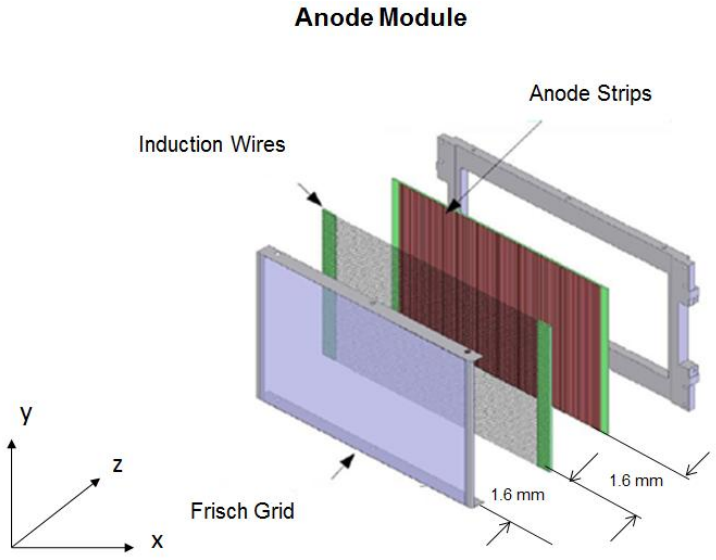

Figure 15 Schematic diagram of anode module.

Specifications in Anode Module	
Electron Drift Length	5.2 mm
Grid Wires Diameter	0.03 mm
Grid Wires Pitch	0.5 mm
Induction Wires Diameter	0.05 mm
Induction Wires Pitch	1.2 mm
Anode Strips Width	1.0 mm
Anode Strip Pitch	1.25 mm
Anode Strips Thickness	0.05 mm

Table 4 Specification of the anode module for the Garfield simulation.

The potential settings used in this thesis are listed in Table 5. The cathode is at -8000 V. The grid is grounded. Then, the electric field in the drift region, $E_{d,}$ is 708 V/cm. The potentials on induction wires and anode strips are 320 V and 1280 V, respectively. The electric field, $E_{1,}$ between the grid wires and the induction wires was 2000 V/cm, which was higher than E_d , and the electric field between induction wire plane and anode plane, $E_{2,}$ was 6000 V/cm, which was three times higher than $E_{1.}$ The increase of the electric field ensures that the electrons pass through the grid and induction wire plane. When 511 keV γ rays interact with the LXe medium, an ionization electron cloud is generated, and electrons in the electron cloud drift towards the anode module and induce current signals on induction wires and anode strips. In Figure 16, the ideal shape of a point – like electron cloud was described. At the time t_a, the point-like electron cloud passes the grid, and it starts to induce a step-like current signal on the induction wires. The induced signal changes its polarity at the moment when the electron cloud passes the induction wires plane. The induced signals are shared by the two or three closet neighboring wires on the wires plane. The amplitude of the induced signal is inversely proportional to the lateral distance from the ionized electron to the induction wires. At time t_b, when the electron cloud passes the wire plane, a step-like current signal with step height proportional to the total charge in the cloud is induced on the anode strips. The electron cloud is eventually collected by the anode strips at time t_c. The position of the electron cloud's center of gravity can be determined by weighting the size of the signal induced on those two nearest wires and one or two strips, which gives the precise X-Y coordinates of any interaction inside the sensitive volume. The third coordinate Z is obtained by measuring the electron drift time relative to the time of the scintillation signal.

Potential Settings on Electrodes of Anode Module	
Cathode	-8000V
Grid	0V
Induction Wires	320V
Anode Strips	1280V

Table 5 Potential settings on electrodes of anode module.

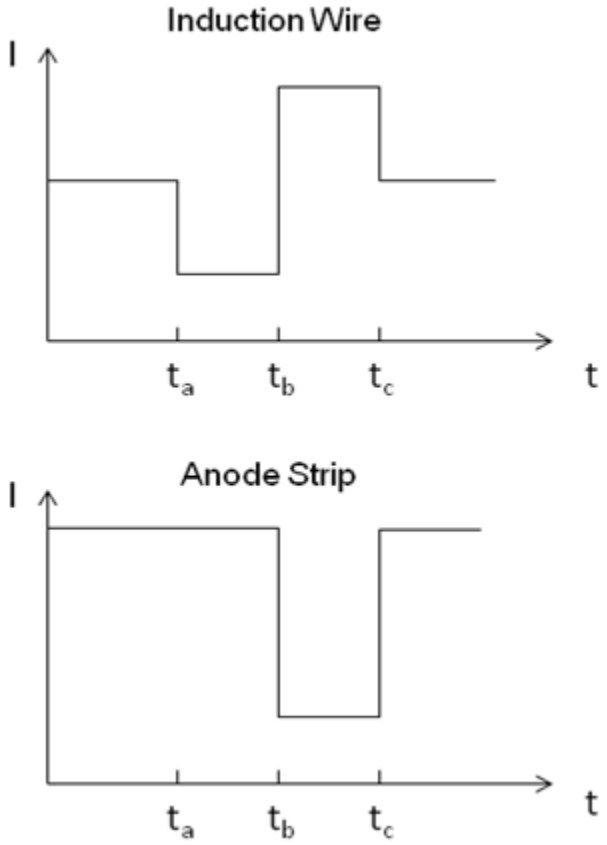

Figure 16 Idealized signal pulse shapes on induction wires and anode strips.

3.2 Simulation of Induced Current Signal

Induced current signals caused by drifting electrons in the induction region were calculated in Garfield (32), which is the most widely used tool for drift chamber simulation. It allows calculation of electric fields, electron and ion drift lines, induced signals, electrostatic wire displacements and many more features of drift chambers.

Garfield begins in a &MAIN section and has seven subsections. The subsections used in this simulation were &CELL, &FIELD, &GAS, &DRIFT and &SIGNAL. &CELL is the first stage of the simulation, in which the specifications of the model and potential setting ups on electrodes are stored. The 3 dimensional model of the anode module in Garfield is shown in Figure 17. The &FIELD section deals with visualization of the electric field in both the drift region and induction region. In the &GAS section, the drift velocity was defined by a table which is shown in Table 6. An interpolation was made to find the drift velocity for the given electric field magnitude in the sector. The &DRIFT section was devoted to displaying the behavior of electrons and ions in the chamber. In the & SIGNAL section, the starting point of a single electron can be set up and the induced current on electrodes are calculated.

Electric Field (V/cm)	Drift Velocity (cm/μs)
100	0.11
400	0.19
1000	0.205
2000	0.220
4000	0.240
6000	0.254
8000	0.258
10000	0.260
12000	0.262
14000	0.263

Table 6 Electric field and its corresponding electron drift velocity in LXe used for current signal calculation in Garfield.

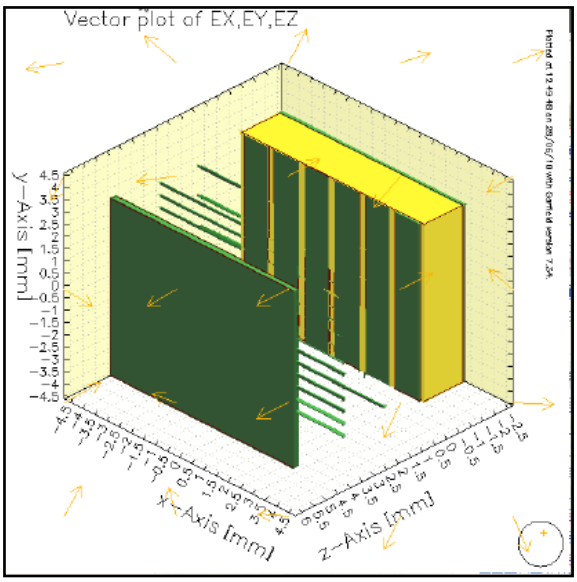

Figure 17 Model of anode module in Garfield. The specifications and potential settings kept the same with the anode module in the prototype.

When an electron starts in the drift region, the induction signals on the electrodes is in the form of y = f (t), where y is current amplitude and t is time. The charge is assumed to follow the calculated trajectory at a saturated speed of around 2mm/μs. The drifting of electrons in

the induction region is shown in Figure 18. It is clearly shown that the electron passed through two wires and reached one of the anode strips on the anode plane. The current signals induced by the single electron on the wires and strips are shown in Figure 19. Compared to the ideal current signal shape discussed above, the simulated wire signals have a bipolar shape with two flat peak parts, which was what we expected. However, due to the imperfection of the shielding of the Frisch Grid, there was induced current on the wires before the electron passed the shielding grid. And the sharp peak on the strip signals was due to the nonuniformity of the electric field near the surface of anode strips. The drift time of the electron in the induction region can be estimated by the difference of the starting time and the ending time of the anode strip signal, which was about 1.5 μs. Because the drift velocity was around 2.2 mm/ μs and the distance between the grid and anode strips is 3.2 mm. The drifting time was as expected. The charges induced on wires and strips were both equal to 1.6×10^{-19}C (the charge of one single electron).

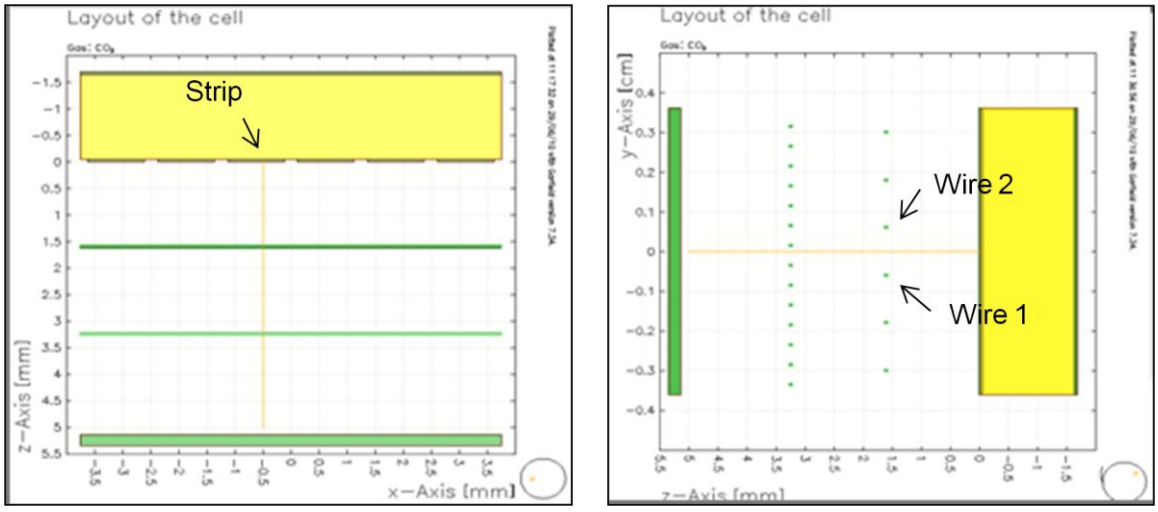

Figure 18 Drifting electron in Garfield simulation model. The solid orange line represents the drifting of the electron.

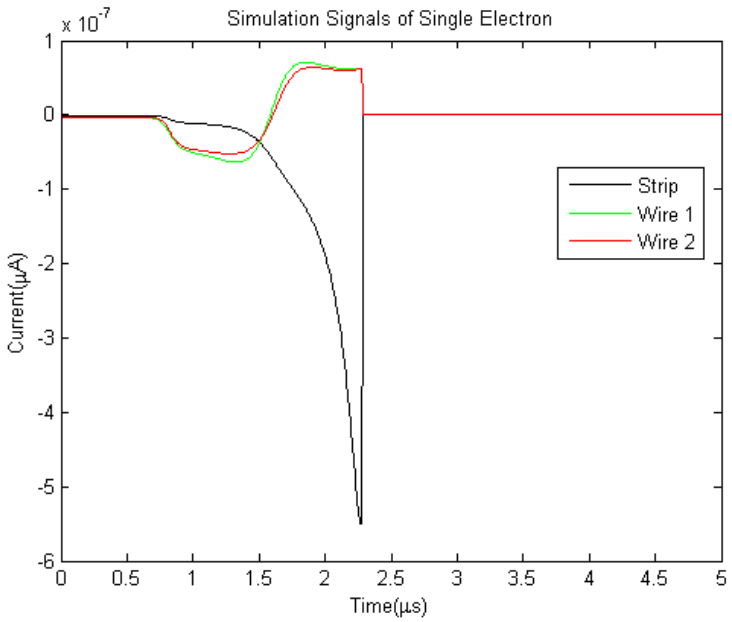

Figure 19 Current signals of single electron on anode strip and induction wires.

3.3 Simulation of Electron Cloud Signal

In Garfield, the current signals induced by a single electron were calculated. However, when a 511 keV γ photon interacts with the LXe detection medium, an electron cloud forms rather than a single electron. Therefore, an electron cloud model was developed for the electron cloud signal simulation. An effective and practical description of the electron cloud left by the 511 keV γ photon interaction can be provided by a uniform distribution of electrons liberated by the primary electron along an electron track (34).

The model of the electron track was developed based on some basic concepts. In this model, the length of the electron track was estimated by a close approximation to the average path length traveled by a charged particle as it slows down to rest, which is called the CSDA range (35). The electron track length was calculated by following equation:

$$\text{Electron track length} = \frac{\text{The CSDA range of 511 keV electrons in LXe}}{\text{Density of LXe}}$$

For electrons of 511keV kinetic energy, the CSDA range is 0.3012 g/cm^2 (36). The density of LXe is 3 g/cm^3. Therefore, the electron track length is roughly 1mm. The orientation of the track is determined by two angles θ and φ, which are described in Figure 20.

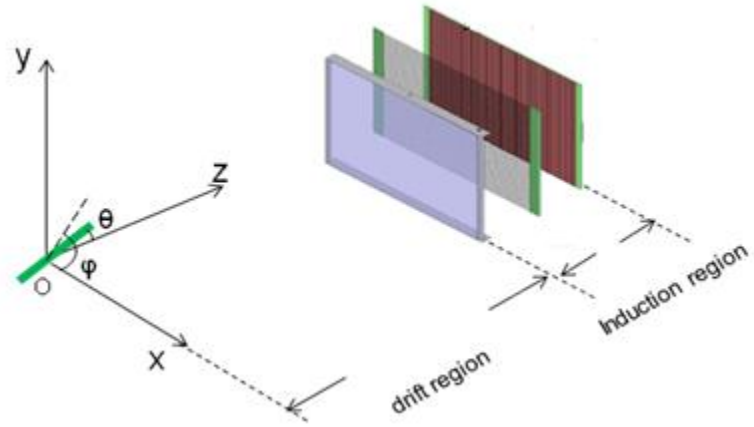

Figure 20 Electron cloud model showing the drift and induction region.

θ is the angle between the track and the drift direction. φ is the angle between x axis and the track's projection on x-y plane. Actually, θ is the angle between the photoelectron and the direction of the incident photon. According to the differential cross section per unit solid angle of photon-absorption for un-polarized photons (37):

$$\frac{d\sigma(E,\theta)}{d\Omega} = \frac{(\sin\theta)^2}{(1-\beta(E)\cdot\cos\theta)^4} \quad [2+D(E)\cdot(1-\beta(E))\cdot\cos\theta)]$$

where E is photon energy. γ (E) and β(E) are electron parameters calculated by:

$$\gamma(E) = 1 + \frac{E}{511} \text{ and,}$$

$$\beta(E) = \sqrt{1-\frac{1}{\gamma(E)^2}} \ ,$$

D(E) can be calculated by (37):

$$D(E) = \gamma(E)\cdot(\gamma(E)-1)\cdot(\gamma(E)-2)$$

Then, for 511keV γ rays, the normalized angular distribution of photoelectrons can be calculated, as shown in Figure 21. From the calculation, the photoelectrons created by 511 keV γ rays have the largest emission probability at 20 degrees. The angle φ is uniformly distributed between 0 and 2π.

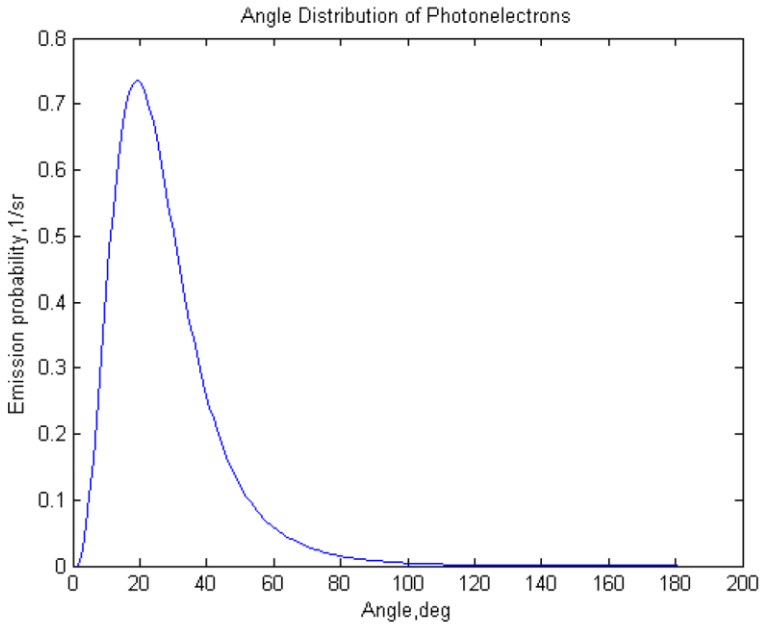

Figure 21 Angular distribution of photoelectrons of 511 keV γ ray interactions with Liquid Xenon.

The number of electrons along the electron track was estimated by the average energy for creating an ion-electron pair in LXe:

$$Q_0 = \frac{E_\gamma}{W}$$

Where E_γ is the energy of the γ ray which is deposited in LXe. W is the average energy to produce an electron ion-pair, which is 15.6 eV. So for 511 keV γ rays, 32000 ionization electrons are generated in the LXe detection medium if the energy of the γ ray is absorbed totally. The 3D starting position of a certain electron along this track can be known as:

$$\begin{cases} x = l \cdot \sin\theta \cdot \sin\varphi \\ y = l \cdot \sin\theta \cdot \cos\varphi \\ z = l \cdot \cos\theta \end{cases}$$

Here X axis is parallel to the induction wires, while Y axis is parallel to anode strips. Z axis is along the drift direction. l is the position of the electron along the electron track, which is uniformly distributed between (-L/2, +L/2). L is the electron track length.

When electrons drift under the applied electric field in the TPC, the electron track diffuses to an electron blob. The spread of the electron blob due to diffusion during the drifting process in the drift region is determined by the transverse diffusion coefficient and drift time. The transverse spread of an electron blob, σ_{D_T}, drifting over a drift time, $t_{d,}$ is given by (38):

$$\sigma_{D_T} = \sqrt{D_T t_d}$$

where D_T is the transverse diffusion coefficient and t_d is drift time. The arrival position of an electron when it reaches the induction region is distributed according to a Gaussian distribution with standard deviation of σ_{D_T}. The electron diffusion coefficient depends on electric field, both in magnitude and direction. The transverse diffusion coefficient, D_T is much larger than the longitudinal diffusion coefficient, D_L in the drift direction. Therefore, the diffusion along the drift direction was ignored in this simulation. A number of papers have reported the experimental results of the transverse diffusion coefficient (39) (40). In (40), the reported transverse diffusion coefficient, D_T, was 34cm^2/s at the electric field of 1kV/cm, and measured with a similar experimental set-up with our lab in 2011. A typical electron blob in this simulation is shown in Figure 22.

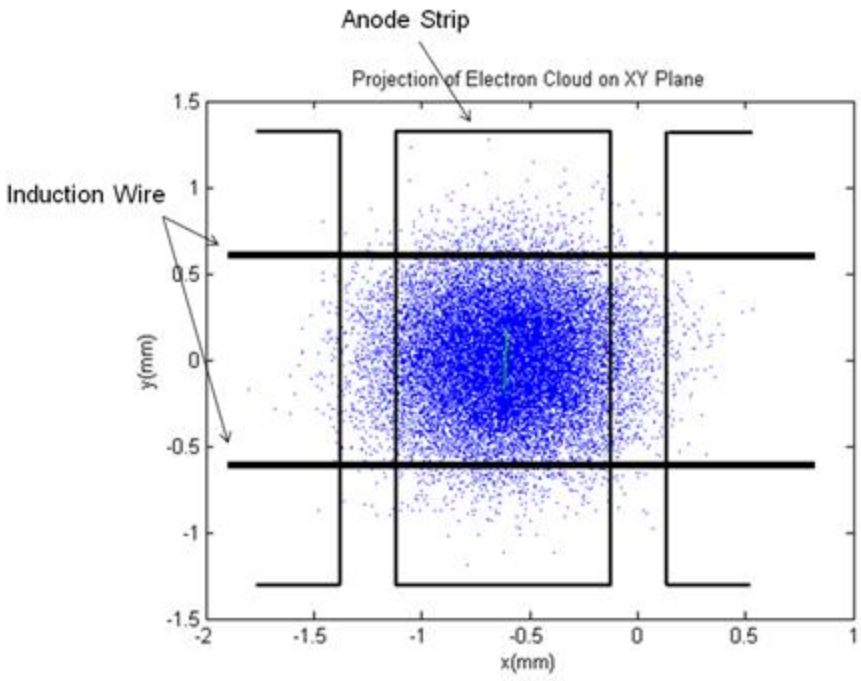

Figure 22 Projection of a typical simulated electron blob on X-Y plane arriving at the anode module. The green track is the original electron track. The center of the electron track is in the middle of one strip and two wires. The diffusion coefficient here is 34cm^2/s. The drift time is 23 μs. The size of the blob was compared to the spacing of wires and the size of the strips.

During the drifting, not all electrons can reach the anode module as collected charges due to electron recombination. The number of electrons which get recombined with positive ions also depends on magnitude of the electric field applied in the drift region. Larger electric field magnitude causes fewer electrons to get recombined. If there is no electric field applied between the cathode and anode in the chamber, 100% of the electrons will recombine with positive ions. The number of electrons which can reach the anode module can be calculated from (29):

$$Q_{e-} = \frac{(1 - Fr^*)E_\gamma}{W}$$

Where Fr* is the electron- ion rec0ombination fraction. At 1 keV/cm electric field, Fr* is 0.29, according to the measurement conducted in 2009 in our lab (41). Around 23000 electrons reached the anode module for a 511keV γ ray event considering the electrons recombination.

The arriving positions of each electron were simulated and recorded in Matlab (33). The position coordinates can be used as the input information for the calculation of induced signals in Garfield. In order to simulate signals induced by the electron blob, the current signal induced by each single electron in this blob needs to be calculated. However, if we calculate the current signal for each electron one by one, it is inefficient and time-consuming. So an algorithm based on a signal map was developed for fast simulation of the induced current signal of the electron blob. Basically, the signal map consists of the signals induced by 100 electrons, which were uniformly distributed in a small area (0.6125 mm * 0.6 mm) on the X-Y plane of anode module. The area was painted in pink in Figure 23. According to the arriving positions of a given electron in that electron blob, its induced current signals were selected from the signal map, which was created by the nearest sampling electron. The sum of the signals induced by all electrons in the electron blob was calculated as the signals of the electron blob. We can expand the sampling area as large as it needed to cover the spread of the electron blob based on the symmetry property of the anode module.

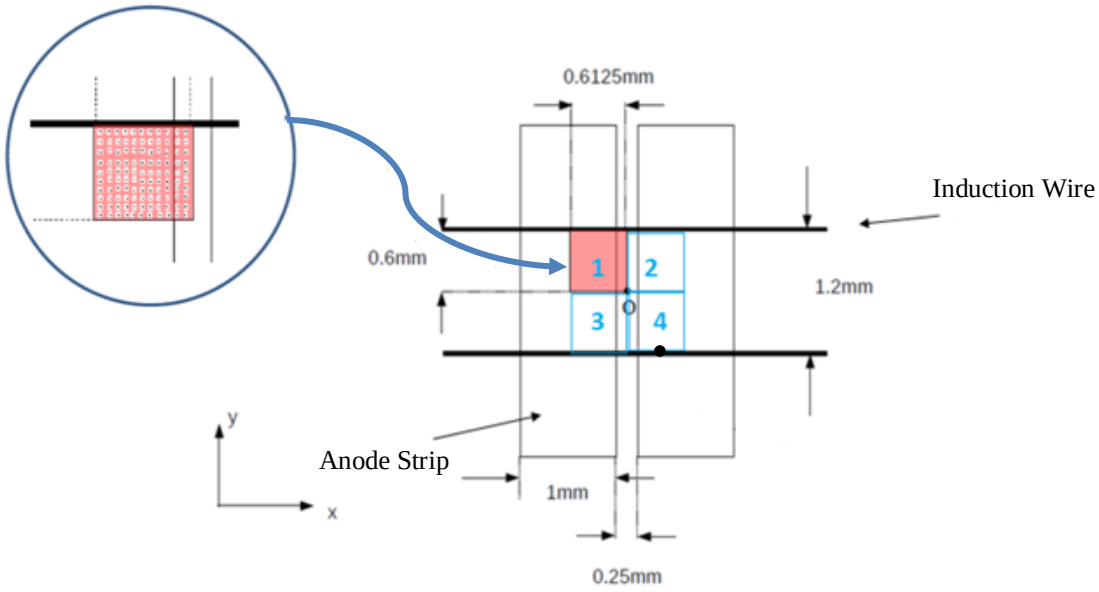

Figure 23 The pink area 1 was sampled by 100 uniformly distributed electrons to generate a signal map. And this area can be symmetrically expanded to area 2, 3, and 4.

In the sector prototype, the current signals induced by electron clouds were amplified by a charge sensitive amplifier. In order to compare the simulated signals to measured signals, the simulated current signal needs to be amplified based on the transfer functions of amplifier connected with the readout in the prototype. The schematic diagram of the circuit and amplifier is described in Figure 24. In order to simulate the correct amplified amplitude of signals, a square voltage pulse with height of 0.3mV was sent into the 'Calin' port for measuring the transfer function of the amplifier. The capacitance of the calibration capacitor C_c is 1.6 pf with 1ns time constant. The voltage pulse caused 0.48 fC charge in the Capacitor C_c and a narrow current pulse with time constant of 1ns generated by the discharging of C_c was sent to the amplifier, and the transfer function of amplifier was the output measured at 'Outport'. Then another voltage pulse with height of 0.1mV was sent to the anode board via the 'SigIn' port. The capacitor C_a stands for the capacitance of the anode board, which was

unknown. The current caused by C_a discharge went though the transmission cable between the detector and amplifier and then was sent in to the amplifier. The transfer function measured in this way represented the correct shape of the amplified signals because it took into account the effect from the transmission line (permeability of 2.5 nH/m) on the signals.

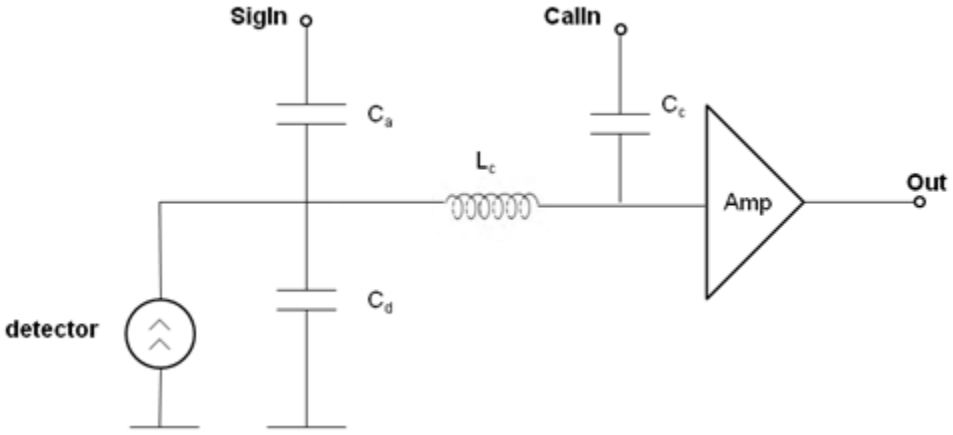

Figure 24 Amplification circuit connected with the detector.

Then the transfer function of the amplifier and the one measured from the anode board are shown in Figure 25.

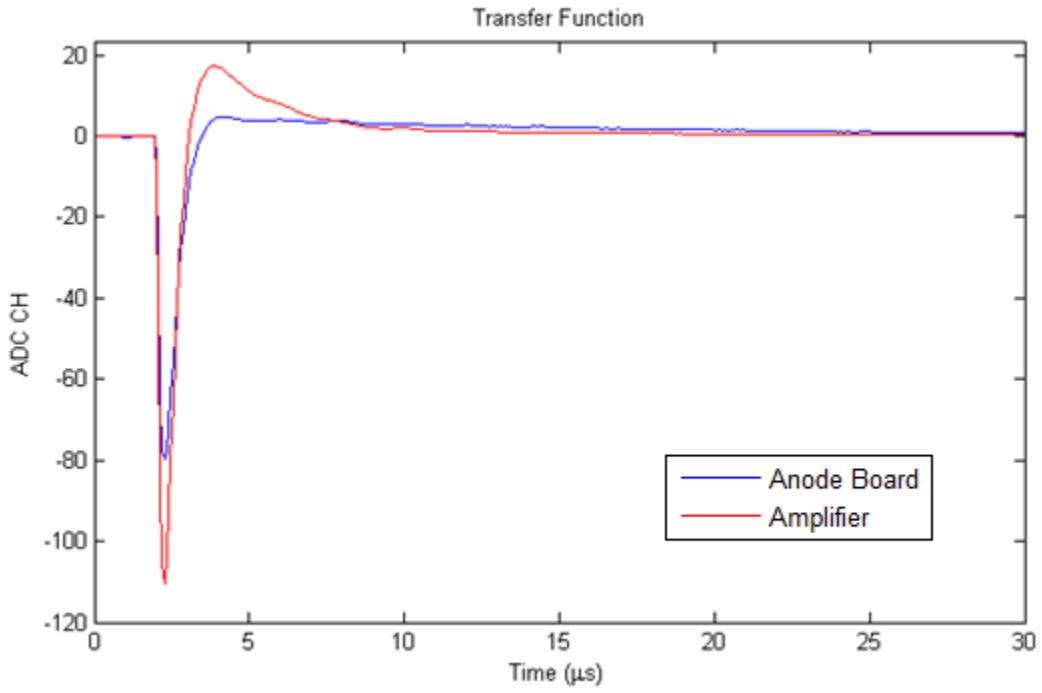

Figure 25 Red line describes the transfer function of the amplifier. The amplification factor was 63.5 mV/fc. The blue line shows that test pulse was sent to the anode board representing the transfer function for simulating the shape of the signals.

The amplified simulated signals of a typical electron cloud generated by 511 keV γ ray are simulated. On the left of Figure 26, the center of the simulated electron cloud was shown as the black spot which is exactly between two wires and in the center of one strip. The dotted blue line describes an approximate boundary of the spread of the electron cloud on the X-Y plane. The drift time was 23 μs, and the drift coefficient was 34cm^2/s. There were 23372 electrons in the electron cloud. 171 electron clouds were simulated, based on the angular distribution of photoelectrons. The average cloud signal is shown on the right of Figure 26.

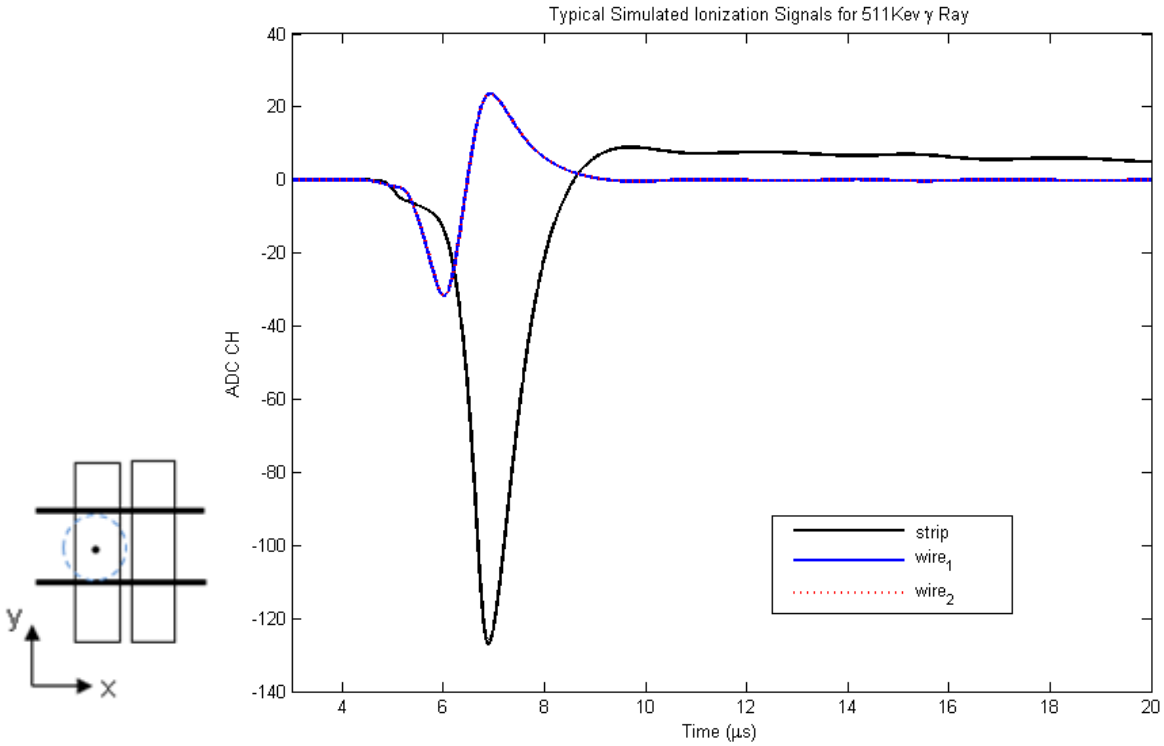

Figure 26 Amplified signals for a typical electron cloud generated by a 511keV γ ray.

3.4 Signal Comparison

3.4.1 Comparison to Template

Firstly, a simulated strip signal was compared to a template, which was the average of measured strip signals. The template represents the standard shape of strip signals with suppressed noise. The comparison result is shown in Figure 27. Since the focus of this comparison was the shape of simulated signals, the amplitude of the simulated strip signal was normalized with the template. From the comparison result, the simulated signal rises earlier than measured signals. This is because in simulation, the shielding grid was made of only one layer of mesh wires; while in the TPC prototype, the shielding gird consists of two layers of mesh wires which were perpendicular with each other, providing better shielding

effect from drifting electrons in the drift region. In addition, the shielding effect of the induction wire plane is not perfect. The early signal on the strip is maximum when the electrons are exactly in between two wires and it is minimum when they arrive immediately above the wires. Therefore, strip signals generated at different positions along Y- axis were averaged for comparing with the template. Except the starting part of the signal, the shape of the simulated strip signal shows very good agreement with the template.

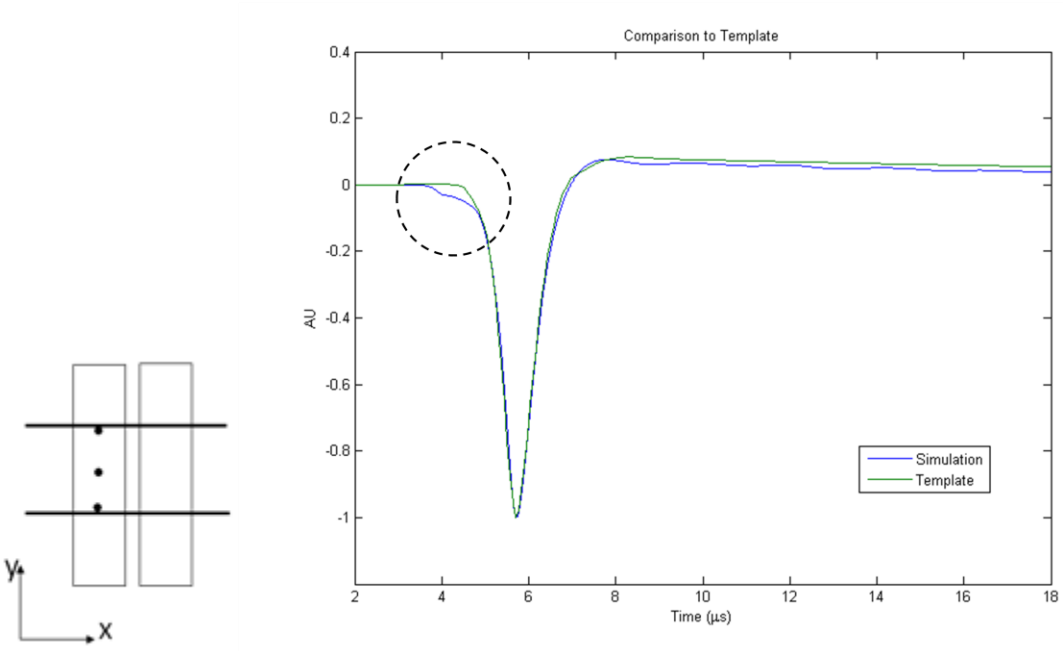

Figure 27 Comparison result between simulated strip signal and template. The part in side of the dotted circle shows the early signal of the simulated signal. On the left, it shows the sampling positions along Y-axis.

3.4.2 Comparison to Signal of Example Event

3.4.2.1 Example Event

The comparison between the simulated signals and measured signals is made in this section. The signals from the detector prototype were measured on July 22, 2011. The experimental set-up consisted of the LXe detector, a ^{22}Na point source and a BriLanCe detector, which are shown in Figure 28. ^{22}Na is a positron-emitting isotope with a long half-life (2.6 years), which is commonly used as an external point-source for PET research. In this measurement, the ^{22}Na source was taped in the center of the window of the cryostat which houses the detector. Two 511 keV back-to-back γ-rays can trigger the chamber in coincidence with the BriLance detector at the opposite side. The signals from the detector were sent to the amplifier, then to waveform digitizer VF48 modules (29). The sampling rate was set to 15 MHz. The APD signals were sent to a current sensitive preamplifier and to a VF48 digitizer module. The sampling rate was set to 60 MHz. The potential settings were the same as the settings in the simulation. The high voltage on the anode strips was 1280 V, and on the induction wires it was 320 V. The Frisch grid was grounded. The cathode was biased at -8000 kV.

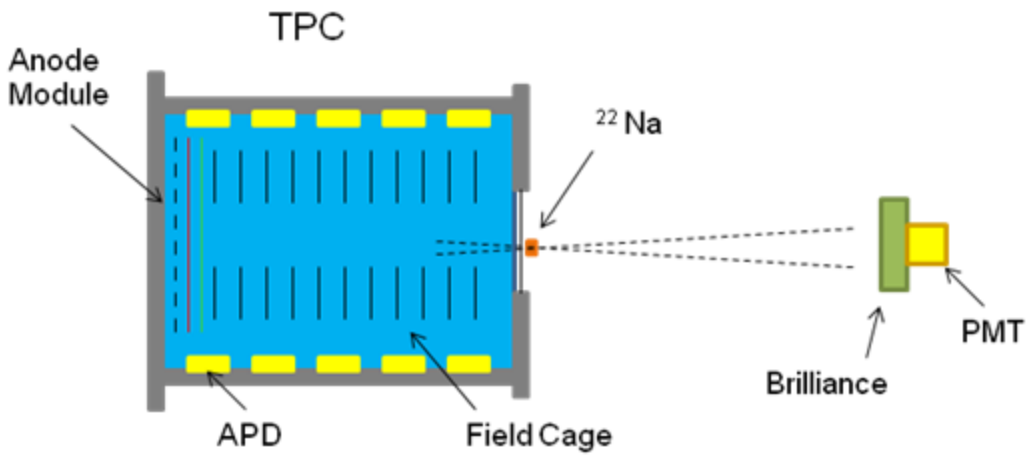

Figure 28 Experimental Set-up for measuring the signals induced by the electron cloud generated by 511 keV γ ray.

An example measured event is shown in Figure 29. In this event, induced current signals were on wire_54, wire_58 and strip_26. The numbering system of wires and strips depended on the channel number in the data acquisition system, rather than their physical positions in the detector. So $wire_{54}$ and $wire_{58}$ were in fact physically neighboring wires. The typical effective noise was about 4 ADC counts which was the measured fluctuation without signal. The major contribution to the noise was the electronic noise from the front-end electronics.

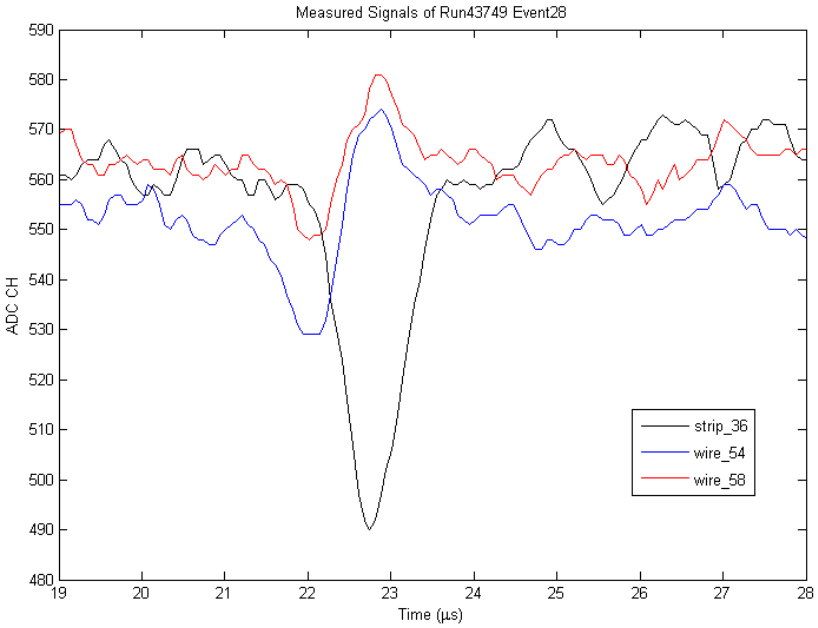

Figure 29 Signals on induction wires and anode strips in Run 43749 Event 28. The black line shows the anode strip signal on strip_36, and the blue and red lines show the induction wire signals on wire_54 and wire_58 individually.

Based on the amplitude on wires and strips, the weighting position of the electron cloud was determined on the X-Y plane. The spacing of strips and wires defined the scale of the coordinate system. Origin point, and positions of strips and wires are described in Figure 31. Since there was only one strip induced by the electron cloud, then the center of the cloud was assumed be in the center of strip_36. Then the weighting position of the center between $wire_{54}$ and $wire_{58}$ was estimated by following equation:

$$\text{Weighting Y position of electron blob} = \frac{\text{Amp\_wire}_{54} \cdot P_{54} + \text{Amp\_wire}_{58} \cdot P_{58}}{\text{Amp\_wire}_{54} + \text{Amp\_wire}_{58}}$$

Where amp_wire_{54} and amp_wire_{58} are the amplitudes of signals on wire_54 and wire_58, P_{58} and P_{54} are their positions on the Y axis. Therefore, the weighting position of the center of

gravity of the electron lob was (-0.6125, 0.1199), which was shown as a black spot in Figure 30.

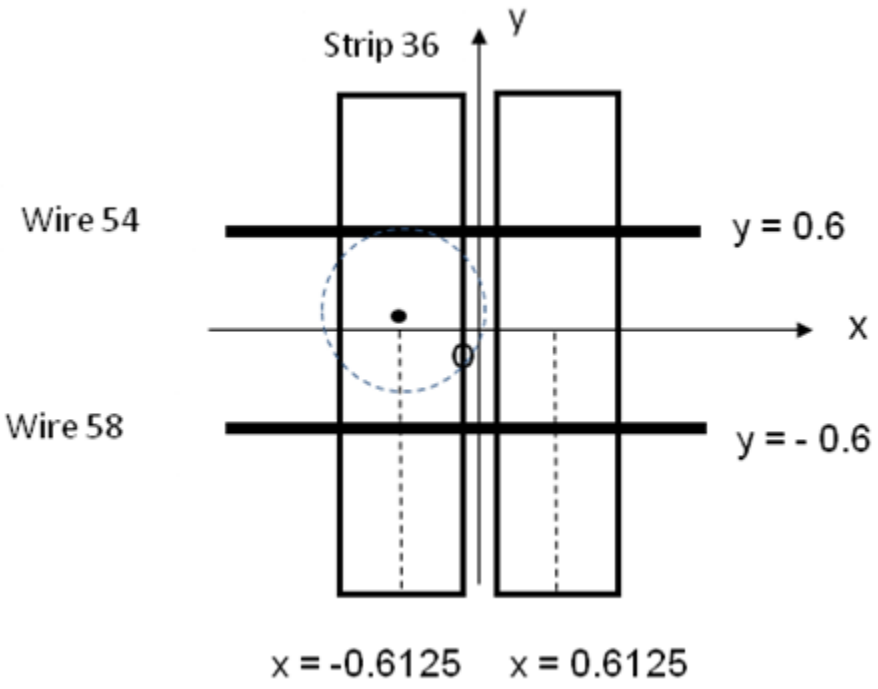

Figure 30 The gravity center of the electron cloud of the example event on X-Y plane.

Drift time, $t_{drift,}$ was measured by the difference of peak times of signals on the strip and APDs:

$$t_{drift} = t_{strip} - t_{APD}$$

where t_{strip} is the time of the peak in the strip, and t_{APD} is the peak time of the APD. For this event, the measured drift time t_{drift} is 22.7 ns.

Simulated electron cloud signals with the same drift time and weighting position of gravity center on the X-Y plane are shown in Figure 31. The signal was averaged from signals of 175 electron clouds, which were generated based on the angular disctribution of 511 keV

photoelectrons. Each cloud include 23372 electrons. Then this average signal was compared to a template and also to the measured signal of the example event.

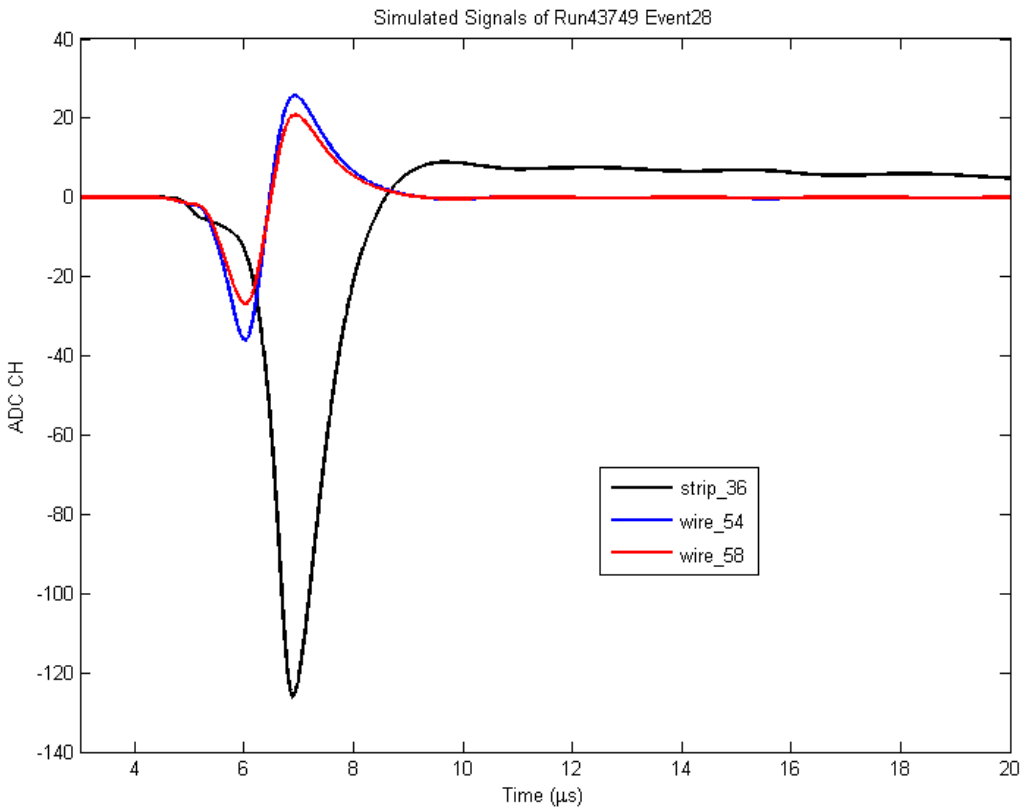

Figure 31 Simulated electron cloud signals of Run43498 Event 28.

3.4.2.2 Signal Comparison

Then the simulated signal was compared to the signal of the example event, as it is shown in Figure 33. Since the attenuation of the electron cloud due to electron attachment was not taken into account in this simulation, the simulated strip signal was normalized with the measured strip signal. And the simulated wire signals were normalized with the same normalization factor. After normalization, the simulated wire signals were smaller than

measured wire signals in amplitude by 14.0% and 10.6%, respectively. Considering the noise level was about 4 ADC ch, which is 9.7% and 12.0% of the wires' amplitude, the results were comparable. Also the time difference of the negative peak and positive peak in the bipolar signals was comparable for the simulated signals and measured ones.

	Simulation		Measurement (ADC CH)
	(w/o Normalization) (ADC CH)	(w/ Normalization) (ADC CH)	
strip_36	126.0	76.0	76.0
wire_54	61.8	38.7	45.0
wire_58	47.8	29.5	33.0

Table 7 Amplitudes of simulated and measured signals.

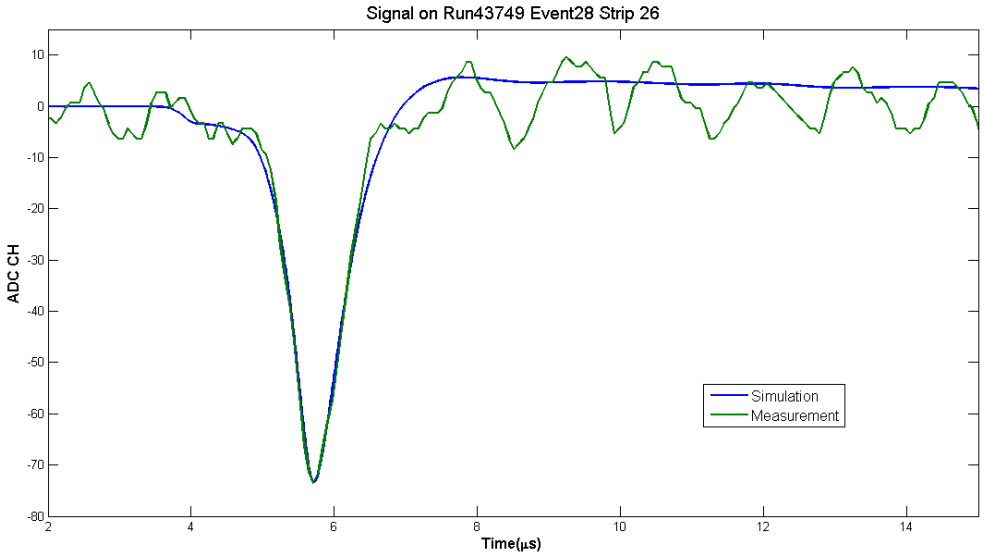
Signal on Run43749 Event28 Strip 26
ADC CH
Time(μs)
Simulation
Measurement

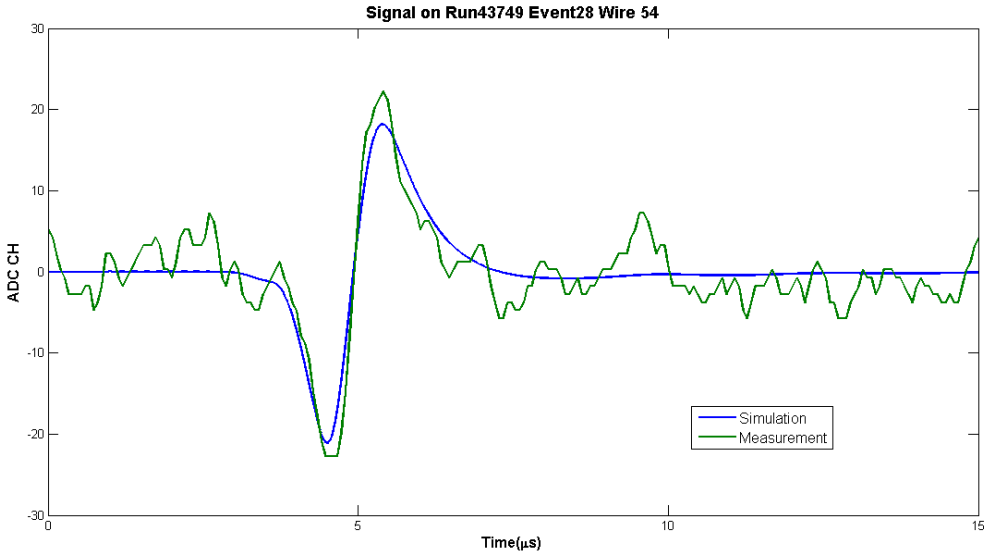
Signal on Run43749 Event28 Wire 54
ADC CH
Time(μs)
Simulation
Measurement

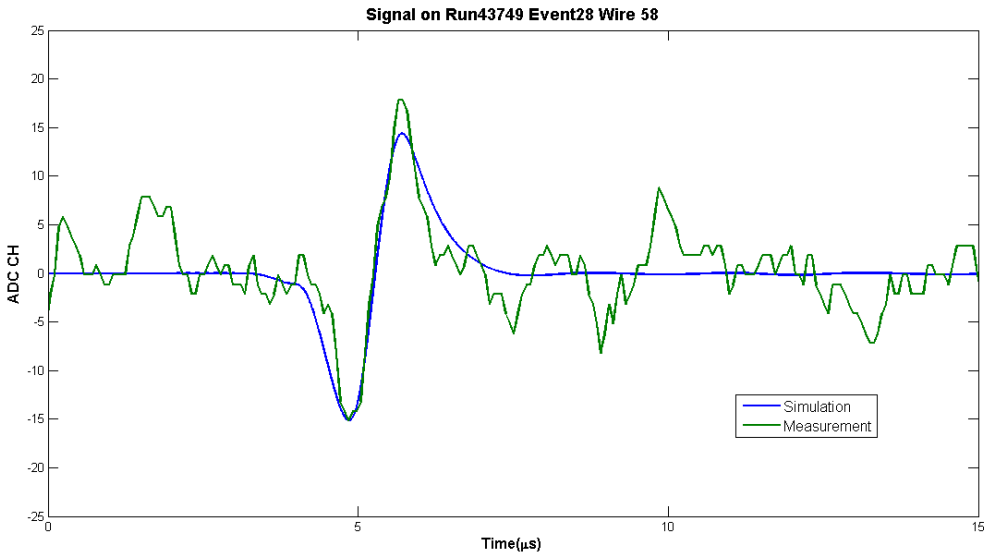

Figure 32 Comparison results between simulated results and measured results for Run437489 Event28. The simulated strip signal was normalized with the measured one. And simulated wire signals were normalized with the same normalization factor.

Chapter 4: Conclusion

A Liquid Xenon PET detector for use in a high resolution micro-PET system is currently under development. Calculation of the electric field and simulation of ionization signals can provide a better understanding of the detector. Finite Element Analysis of the electric field in single sectors of the prototype showed good uniformity and a deviation map of the whole volume was determined for further calibration purposed. The calculation was performed with a script (comi.file), which can be easily modified for calculation of detectors with different geometries. How much the deviation map can improve the position reconstruction of the interaction point is also interesting for further study.

The simulation of the signals measured from the LXe detector prototype was made. The simulation results were in good qualitative agreement with the measurement signals. This method was found to be promising to provide a framework to simulate the ionization signals in the LXe PET detector. However, the simulation model could not fully represent the reality and needs improvements in the future. Firstly, a straight trajectory of the primary photoelectron and secondary ionized electron uniformly distributed along the electron track was assumed. As a matter of fact, the trajectory is not a straight line due to scattering, and also the largest part of the energy of the primary photoelectron is deposited at the end of the track rather than uniformly distributed along the trajectory. Moreover, the attenuation of the electron cloud due to electron attachment during the drift was not taken into account. Therefore, future work is required for improving this method.

Bibliography

1. Bengel FM et al. Cardiac Positron Emission Tomography. Journal of the American College Cardiology, Vol.54, No.1, 2009.
2. P K Morrish et al, Measuring the rate of progression and estimating the preclinical period of Parkinson's disease with [^{18}F] dopa PET, J Neurol Neurosurg Psychiatry 1998;64:P314–319.
3. Niraj K. Doshi et al, Design and evaluation of an LSO PET detector for breast cancer imaging, Med. Phys. 27 1535 (2000).
4. T. B. Lynch, PET/CT in Clinical Practice, Springer 2007.
5. Tom K Lewellen, Recent developments in PET detector technology, Phys. Med. Biol. 53 (2008).
6. Miles N.Wernick et al, The fundamentals of PET and SPECT, Elsevier Inc. 2004.
7. M. Charlton, et al, Positron Physics, Cambridge University Press. 2001.
8. Charles Mcconnell Clement, Simulations of a high-resolution micro-pet system based on liquid xenon, Master thesis, the University of British Columbia, 2011.
9. Positron Emission Tomography: Basic Sciences, Springer, 2004.
10. Valentino Bettinardi et al, Performance evaluation of the new whole-body PET/CT scanner: Discovery ST, European Journal of Nuclear Medicine and Molecular Imaging Vol. 31, No. 6, June 2004.
11. Hans Herzog et al, NEMA NU2-2001 Guided Performance Evaluation of Four Siemens ECAT PET Scanners, IEEE Transactions on Nuclear Science, Vol. 51, No. 5, October 2004.

12. Suleman Surti et al, Performance of Philips Gemini TF PET/CT Scanner with Special Consideration for Its Time-of-Flight Imaging Capabilities, J Nucl Med 2007; 48:471–480.
13. K. Ziemons et al, The ClearPET project: development of a 2nd generation high-performance small animal PET scanner, Nuclear Instruments and Methods in Physics Research A 537 (2005) 307–311.
14. Y-C Tai et al, MicroPET II: An Ultra-high Resolution Small Animal PET System,0-7803-7636-6/03/2003 IEEE.
15. D. L. Snyder et al, "A mathematical model for positron-emission tomography systems having time-of-flight measurements," IEEE Trans. Nucl. Sci., vol. NS-28, pp. 3575–3583, June 1981.
16. W. W. Moses, Time of Flight in PET Revisited, IEEE Transactions on Nuclear Science, Vol. 50, No. 5, Oct. 2003.
17. Hugo W A M de Jong, Performance evaluation of the ECAT HRRT: an LSO-LYSO double layer high resolution, high sensitivity scanner, 2007 Phys. Med. Biol. 52 1505.
18. Tsuda, T, A four-Layer depth of interaction detector block for small animal PET, Nuclear Science, IEEE Transactions on Issue Date: Oct. 2004 Vol. 51 Issue:5 pp. 2537 – 2542.
19. L.Lavoie, Liquid xenon scintillators for imaging of positron emitters, Med. Phys., Vol.3, pp.283-293, 1976.
20. H.Zaklad et al, A liquid xenon radioisotope camera, IEEE Trans. on Nucl. Sei., NS-19, pp.206-212, 1972.

21. Tadayoshi Doke et al, Present status of liquid rare gas scintillation detectors and their new application to gamma-ray calorimeters, Nuclear Instruments and Methods in Physics Research A 420 (1999) 62D80.
22. F. Xu. “Development of a LXe-TPC Compton telescope for gamma-ray astronomy”, PhD dissertation. Columbia University.
23. P. Amaudruz et al, Investigation of Liquid Xenon Detectors for PET: Simultaneous Reconstruction of Light and Charge Signals from 511 keV Photons, 2007 IEEE Nuclear Science Symposium Conference Record.
24. P. Amaudruz et al, Design and Performance of Liquid Xenon Detectors for PET, 2008 IEEE Nuclear Science Symposium Conference Record.
25. Saha, Gopal B. Basics of PET Imaging: Physics, Chemistry, and Regulations, Springer, 2010.
26. Opera 3D website. http://www.cobham.com/.
27. ROOT website. http://root.cern.ch/.
28. L. S. Miller, S. Howe, and W. E. Spear, Charge Transport in Solid and Liquid Ar, Kr, and Xe,Phys. Rev. 166 (1968), 871.
29. A. Miceli, Liquid Xenon Detectors for Positron Emission Tomography, Journal of Physics: Conference Series 312 (2011).
30. A. Miceli, Group meeting note, Sep. 2009.
31. Michael Lozinki, Electric Field Calculation for a Prototype Liquid Xenon PET, Bachelor thesis, 2008.
32. Garfield website. http://garfield.web.cern.ch.
33. Matlab website: http://www.mathworks.com/products/matlab/.

34. Walter Blum et al, Particle Detection with Drift Chambers, Springer 2008.

35. Ervin B. Podgorak, Radiation Physics for Medical Physicists, Springer 2010.

36. http://www.pd.infn.it/~conti/LXe.html, Enrico Conti's Liquid Xenon Page, Last update: 21 Jun 2010.

37. L. Kurchaninov, writing note (Private communication).

38. E. Aprile et al, Liquid Xenon Detectors for Particle Physics and Astrophysics, Rev. Mod. Phys. 82, 2053 – 2097 (2010).

39. Tadayoshi Doke, Recent developments of liquid xenon detectors, Nuclear Instruments and Methods in Physics Research Volume 196, Issue 1, 1 May 1982, Pages 87-96.

40. W.-T. Chen et al, Measurement of the transverse diffusion coefficient of charge in liquid xenon, arXiv:1109.3300.

41. P. Amaudru et al, Simultaneous reconstruction of scintillation light and ionization charge produced by 511 keV photons in liquid xenon: potential application to PET, Nuclear Instruments and Methods in Physics Research A 607 (2009) 668–676.

Appendix A Spacing of the electrodes of the model in Opera 3D

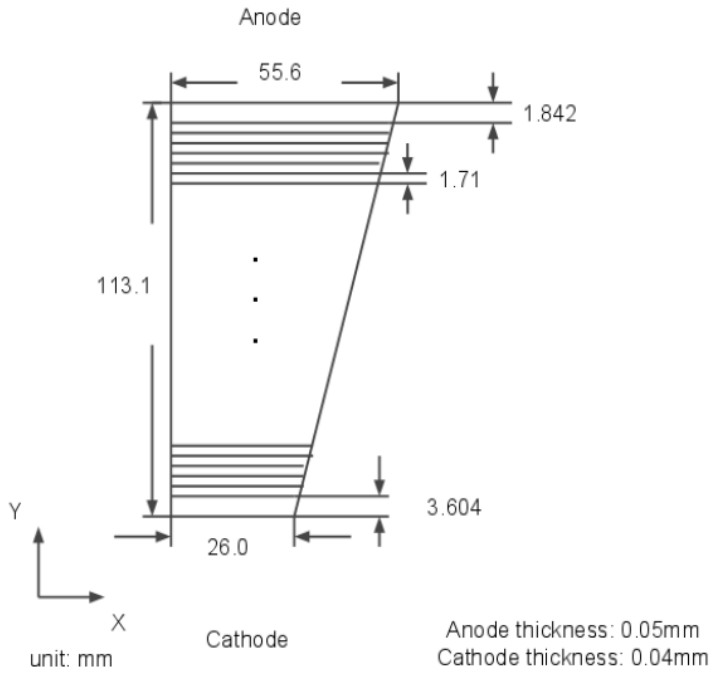

Figure 33 The spacing of the 64 field cage wires, the cathode and the anode in the planes of the APDs.

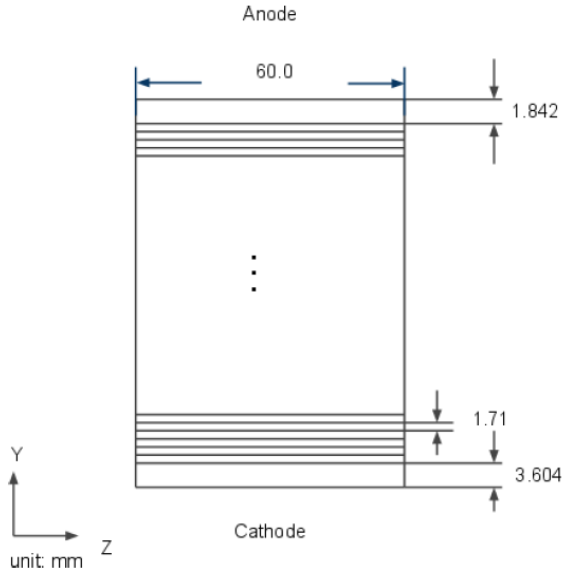

Figure 34 The spacing of the 64 field cage strips, the cathode and the anode on the faces of the sector perpendicular to the APDs.